Pergamon

PII S0016-7037(00)00853-5

Surface complexation and precipitate geometry for aqueous Zn(II) sorption on ferrihydrite I: X-ray absorption extended fine structure spectroscopy analysis

G. A. WAYCHUNAS,[1,]* C. C. FULLER,[2] and J. A. DAVIS[2]

[1]E. O. Lawrence Berkeley National Laboratory, Earth Sciences Division, Geochemistry Department, MS 70-108B, Berkeley, CA 94720, USA
[2]U.S. Geological Survey, Water Resources Division, Menlo Park, CA 94025, USA

Abstract—"Two-line" ferrihydrite samples precipitated and then exposed to a range of aqueous Zn solutions (10^{-5} to 10^{-3} M), and also coprecipitated in similar Zn solutions (pH 6.5), have been examined by Zn and Fe K-edge X-ray absorption spectroscopy. Typical Zn complexes on the surface have Zn-O distances of 1.97(.02) Å and coordination numbers of about 4.0(0.5), consistent with tetrahedral oxygen coordination. This contrasts with Zn-O distances of 2.11(.02) Å and coordination numbers of 6 to 7 in the aqueous Zn solutions used in sample preparation. X-ray absorption extended fine structure spectroscopy (EXAFS) fits to the second shell of cation neighbors indicate as many as 4 Zn-Fe neighbors at 3.44(.04) Å in coprecipitated samples, and about two Zn-Fe neighbors at the same distance in adsorption samples. In both sets of samples, the fitted coordination number of second shell cations decreases as sorption density increases, indicating changes in the number and type of available complexing sites or the onset of competitive precipitation processes. Comparison of our results with the possible geometries for surface complexes and precipitates suggests that the Zn sorption complexes are inner sphere and at lowest adsorption densities are bidentate, sharing apical oxygens with adjacent edge-sharing $Fe(O,OH)_6$ octahedra. Coprecipitation samples have complexes with similar geometry, but these are polydentate, sharing apices with more than two adjacent edge-sharing $Fe(O,OH)_6$ polyhedra. The results are inconsistent with Zn entering the ferrihydrite structure (i.e., solid solution formation) or formation of other Zn-Fe precipitates. The fitted Zn-Fe coordination numbers drop with increasing Zn density with a minimum of about 0.8(.2) at Zn/(Zn + Fe) of 0.08 or more. This change appears to be attributable to the onset of precipitation of zinc hydroxide polymers with mainly tetrahedral Zn coordination. At the highest loadings studied, the nature of the complexes changes further, and a second type of precipitate forms. This has a structure based on a brucite layer topology, with mainly octahedral Zn coordination. Amorphous zinc hydroxide samples prepared for comparison had a closely similar local structure. Analysis of the Fe K-edge EXAFS is consistent with surface complexation reactions and surface precipitation at high Zn loadings with little or no Fe-Zn solid solution formation. The formation of Zn-containing precipitates at solution conditions two or more orders of magnitude below their solubility limit is compared with other sorption and spectroscopic studies that describe similar behavior. *Copyright © 2002 Elsevier Science Ltd*

1. INTRODUCTION

1.1. Aqueous Zn^{2+} Complexes and Hydrous Ferric Oxide Sorption Isotherm

Although Zn^{2+} aqueous chemistry has been examined by a number of workers, there remain questions as to the Zn complexes stable at high pH values (Cain et al., 1987; Pandya et al., 1995) and to the type of complexes stable on mineral surfaces. Kinniburgh and Jackson (1982) and Benjamin and Leckie (1981) have shown that the isotherm for sorption of Zn^{2+} on hydrous ferric oxide (HFO) at pH 6.5 deviates significantly from Langmuir behavior at relatively low surface coverages (log[Zn] = −3), where [Zn] indicates the surface concentration as total Zn/total Fe), with complex behavior observed in the range (−3 < log[Zn] < −1)). The shape of the isotherm (Fig. 1) has been interpreted as indicative of the beginnings of surface precipitation despite total zinc concentrations orders of magnitude below the level suspected for the precipitation of $Zn(OH)_2$ (Dzombak and Morel, 1986). Experimental photoelectron spectroscopy (XPS) results on dried samples of HFO

with sorbed zinc also indicate that $Zn(OH)_2$ or some phase with similar valence levels precipitates below the expected saturation level (Harvey and Linton, 1984). Other workers have postulated that Zn^{2+} precipitates with or on iron oxides from natural solutions or within soils under appropriate conditions (Jenne, 1968; Stanton and Burger, 1970; Lindsay, 1979; O'Day et al., 1998). In all of these cases, the nature of the precipitation or relevant sorption complex has not been characterized on a molecular level. Zn^{2+} should be present in aqueous solutions of moderate to low Zn^{2+} concentration and low to moderate pH mainly as a hexa- or perhaps hepta-aqua coordinated specie (Baes and Mesmer, 1976; Tossell, 1991; Fig. 2, I). X-ray absorption extended fine structure spectroscopy (EXAFS) studies of Zn-H_2O coordination in dilute chloride solutions at moderate pH have verified this geometry and indicated Zn-O distances of 2.08 to 2.11 Å (Parkhurst, 1985). Monte Carlo simulations of the Zn^{2+}-H_2O system showed two shells of waters about the average Zn^{2+} ion, the first with mean distance 2.05 Å having ~5.6 waters, and the second at 2.25 Å, having ~1 water (Yongyai et al., 1991). About half of the Zn^{2+} ions have six first-neighbor water molecules in this simulation. At pH values of near 9.0, where some hydrolysis of the Zn^{2+} is expected, Wegmüller (1987) has postulated physisorption of

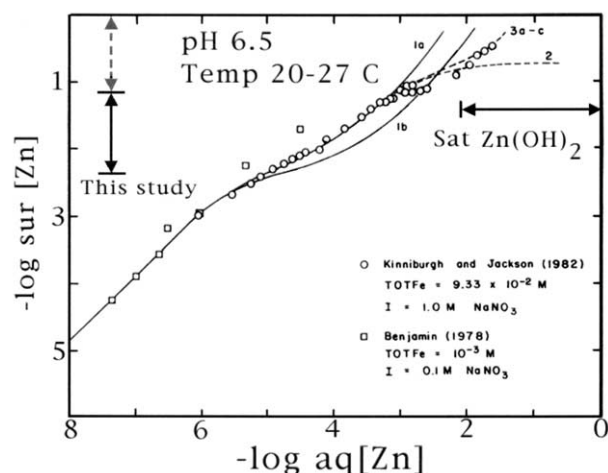* Author to whom correspondence should be addressed (gawaychunas@lbl.gov).

Fig. 1. Sorption profiles for aqueous Zn on ferrihydrite (past work); the solid vertical arrow indicates the abscissa range for most samples in this study. The dashed arrow indicates the range explored with limited samples. After Dzombak and Morel (1986).

$Zn(OH_2)_4(OH)_2$ neutral species on several mineral and synthetic substrates and suggested that a monomolecular surface layer is formed at saturation. Infrared analysis further suggested that Zn-O-Zn coupling occurs in the sorbed layer and is similar to that found in crystalline α-$Zn(OH)_2$ (i.e., octahedrally coordinated Zn^{2+} with Zn-O distances of ~2.13 Å and Zn-Zn distances of ~3.14 Å). Hence, a type of precursor state to a three-dimensional precipitate is postulated to form initially.

In the present work, we examine ferrihydrite samples prepared at pH 6.5 both in the presence of aqueous Zn^{2+} (coprecipitation samples) and exposed to aqueous Zn^{2+} only after precipitation and a short aging period (adsorption samples). At the concentration levels of the study and this pH value, aqua-coordinated Zn^{2+} aqueous species are expected to greatly dominate over hydrolyzed species (Baes and Mesmer, 1976). The sorption coverages were selected to bracket the range of the sorption isotherm of Kinniburgh and Jackson (1982), who proposed that surface precipitation occurred (Fig. 1). The data of Benjamin (1978) are also shown in Figure 1.

1.2. Zn^{2+} Coordination and Crystal Chemistry

Zn^{2+} crystal chemistry is of particular interest because of the variations in Zn coordination geometry observed in stable crystalline compounds (Wells, 1984; Robert and Gasperin, 1985). Not only does Zn^{2+} occur in 4, 5, 6, and 7-oxygen coordinated sites, but it may occupy several of these sites in a single phase. A case in point is hydrozincite, $Zn_5(OH)_6(CO_3)_2$, which is the stable zinc phase in air-saturated water at the Earth's surface (Schindler et al., 1969; Zachara et al., 1989). Zn^{2+} occurs in both tetrahedral and octahedral coordination in hydrozincite in the ratio of 2:3, respectively. In this structure, the mean tetrahedral Zn-O distance is 1.96 Å, whereas the mean octahedral Zn-O distance is 2.10 Å. The hydrozincite structure is based on layers of edge-sharing (ES) $Zn(O,OH)_6$ octahedra with periodic vacancies. Zn tetrahedra are connected to each side of these octahedral holes (Ghose, 1964; Fig. 2, XVII and XVIII). Several other mineral and inorganic materials

have related structures, among them namuwite $[(Zn,Cu)_4SO_4(OH)_6 \cdot 4H_2O]$ (Groat, 1996; Fig. 2, XVI), sclarite $[(Zn,Mg,Mn)_4Zn_3(CO_3)_2(OH)_{10}]$ (Grice and Dunn, 1989; Fig. 2, XIV and XV), simonkolleite $[Zn_5(OH)_8Cl_2 \cdot H_2O]$ (Allman, 1968), $Zn_2Mo_3O_8$ (McCarroll et al., 1957; Ansell and Katz, 1966), and bechererite $(Zn,Cu)_6Zn_2(OH)_{13}[(S,Si)(O,OH)_4]_2$ (Giester and Rieck, 1996). Other structures not having well-defined layers but also with octahedral and tetrahedral Zn include γ-$Zn_3(PO_4)_2$ (Calvo, 1963), β-$Zn_3(PO_4)_2$ (Stephens and Calvo, 1967), and $Zn(OH)_2 \cdot ZnSO_4$ (Iitaka et al., 1962). Layer structures with Zn^{2+} only having octahedral coordination have also been reported. For example, the lamellar hydroxides $Zn_2Cr(OH)_6X \cdot nH_2O$, where X is an anion or polyanion, appear quite stable (Boehm et al., 1977; DeRoy et al., 1985), and hydrotalcite structures $[Mg_6Al_2(OH)_{16}CO_3 \cdot 4H_2O]$ containing major amounts of Zn^{2+} have also been prepared (Porta et al., 1996). Several nitrate-hydroxides of zinc also have related structures (Louer et al., 1973) A common aspect of all the layer structures is the occurrence of a brucite-like layer with ES $Zn(O,OH)_6$ octahedra (Fig. 2, XII and XIII).

Zn^{2+} forms a number of basic hydroxides, most having tetrahedrally coordinated Zn^{2+} (Fig. 2, II) and structures analogous to silica (SiO_2) polymorphs—for example, the ε and γ forms (Schnering, 1964; Christensen, 1969), all with corner-sharing (CS) tetrahedra. However, the α form noted above is reported to have the brucite or CdI_2 planar structure consisting of sheets of $Zn^{2+}(OH)_6$ ES octahedra (Feitknecht, 1938; also discussed by Wegmüller, 1987), with the individual sheets connected only by electrostatic forces. Several of the forms of $Zn(OH)_2$ are difficult to synthesize, producing poor X-ray diffraction patterns and often crystallizing as a mixture of zinc compounds. Consequently, many zinc hydroxides have poorly defined or unknown structures (e.g., the minerals sweetite and ashoverite). There is thus incomplete information available as to the overall stability and crystal chemistry of Zn hydroxide structures. The tendency for Zn^{2+} to inhabit multiple coordination environments does follow from the ionic radius, which is intermediate between so-called radius ratio predictions for tetrahedral and octahedral coordination, and the tendency to form more covalent bonds than other divalent transition elements (Wells, 1984). The diversity of hydroxide phases and the difficulty in synthesizing them also suggest the importance of kinetic factors in their existence.

Given its complex crystal chemistry, Zn^{2+} could interact with the ferrihydrite and Fe^{3+} oxyhydroxide surfaces in a number of ways, some of them simultaneously. Zn^{2+} may replace Fe^{3+} in octahedral coordination at the surface, with charge imbalances corrected by additional surface protonation. This process would tend to be favored at lower pH values, so that a change in surface geometry might occur with increasing pH. Solid solution formation, wherein Zn^{2+} replaces Fe^{3+} within the ferrihydrite structure during coprecipitation, would require more complete modifications of the structure—that is, a defect solid solution wherein OH^- replaces O^{2-} or there are systematic oxygen vacancies. Zn^{2+} can also be sorbed as one or more aqua- or partially hydrolyzed complexes. Such complexes could be either inner or outer sphere and could take a variety of forms. Zn^{2+} aqueous complexes could also react with Fe^{3+} near the mineral surface to form tetrahedral, octahedral, or other mixed coordination complexes. Franklinite,
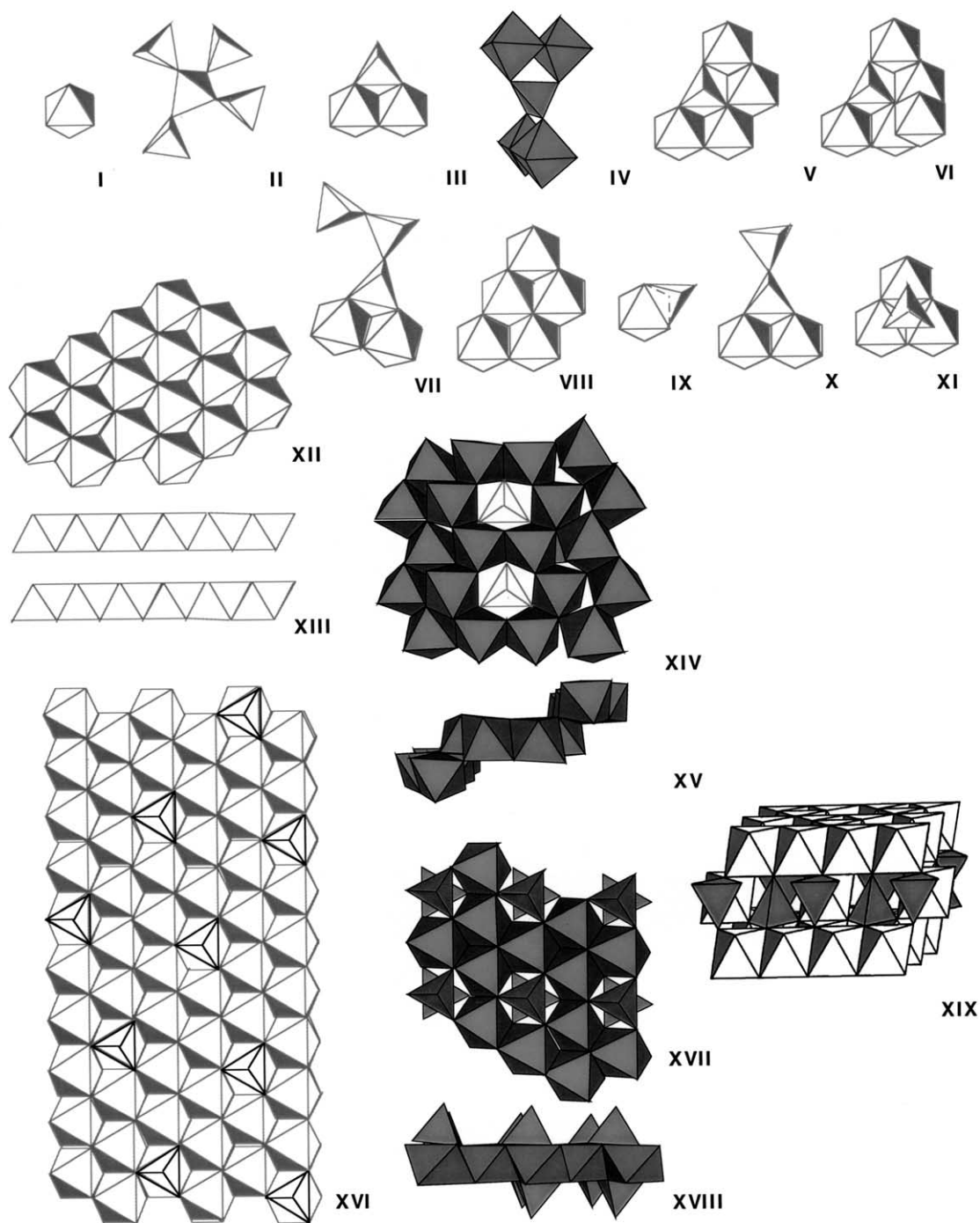
Fig. 2. Types of Zn^{2+} sorption, coprecipitation, and model compound structures. (I) Isolated octahedral complex; form of equilibrium aqueous Zn^{2+}. (II) Tetrahedral Zn sharing vertices; the form of several $Zn(OH)_2$ polymorphs. (III) Bidentate tetrahedral Zn sharing vertices with ES $Fe^{3+}O_6$ units. (IV) Polydentate version of structure III. (V) Planar polydentate cluster. (VI) Another type of polydentate cluster showing increased Zn-Fe next-nearest neighbor. (VII) Extended polymerization of $Zn(OH)_2$ on a bidentate cluster. (VIII) Octahedral Zn substituting into a planar $Fe^{3+}O_6$ structure. (IX) Edge sharing Zn tetrahedra on a $Fe^{3+}O_6$ polyhedron. (X) Bidentate cluster as in structure III with added polymerizing tetrahedral Zn^{2+}. (XI) One type of outer-sphere tetrahedral Zn complex. The oxygens on the vertices of the tetrahedral complex reside just above the midpoint of triads of oxygens on $Fe^{3+}O_6$ faces. (XII) Brucite structure for $Zn(OH)_2$, also known as α-$Zn(OH)_2$. (XIII) Structure XII seen from the side showing nonbonded layers. (XIV) Part of the structural motif of sclarite. (XV) Side view of sclarite structure. (XVI) View of one layer of the namuwite structure. (XVII) Part of the layer in the hydrozincite structure showing octahedral vacancies topped with tetrahedral units. All polyhedra filled with Zn^{2+}. (XVIII) Side view of hydrozincite structure unit shown in XVII. (XIX) Franklinite structure showing octahedral Fe^{3+} layers alternating with mixed Zn^{2+} tetrahedra and Fe^{3+} octahedra layers.

$ZnFe_2O_4$, is a spinel normally formed under high-temperature conditions but could possibly form from a ferrihydrite dissolution reaction in a Zn^{2+}-containing solution (Reddy et al., 1988; Sadiq, 1991). The structure of franklinite is shown in Figure 2, XIX. Finally, isolated or surface-catalyzed precipitation of a Zn^{2+} phase, such as a Zn hydroxide, is also possible. A set of possible surface complexes are depicted in Figure 2 (III to XI), including inner-sphere complexes (III, IV, V, VI, and VIII), mixed precipitate-sorption complexes (VII and X), an ES inner-sphere complex (IX), and one type of outer-sphere complex (XI).

Most of the possible outcomes of Zn^{2+} interaction with ferrihydrite can be examined and ruled on with the structural information provided by X-ray absorption spectroscopy (XAS) methods. XAS analysis involving near edge structure (XANES) and extended fine structure (EXAFS) yields local coordination numbers, ligand types, and interatomic distances that are difficult to obtain for noncrystalline precipitate or sorption-complex structures. Only the selectivity of XAS methods can yield such direct structural information, especially for dilute complexes. For species such as Zn^{2+}, where visible spectroscopy and ESR methods cannot be used and nuclear magnetic resonance or Mössbauer methods are extremely difficult, XAS is an essential tool.

Zn-O distances are, on average, good predictors of the Zn oxygen coordination (Table 1 and Fig. 3). Similarly, Zn-Zn and Zn-Fe distances in known structures appear to have particular ranges associated with tetrahedral/tetrahedral, octahedral/tetrahedral, or octahedral/octahedral polyhedron ES and CS within the structure (Table 1, Fig. 4). Many types of feasible surface adsorption complexes also should have predictable Zn-Fe distances. Hence, EXAFS analysis, which generally yields accurate (to about 1%) absorber-backscatterer near neighbor and next-nearest neighbor distances, should be useful in reducing the number of possible surface reactions. Additionally, there are systematic changes in the XANES that aid in characterizing Zn^{2+} coordination number and Zn–second neighbor metal ion ordering and topology. Thus, many recent investigations use EXAFS and XANES analysis (often referred to together as XAFS) for surface complexation characterization. A detailed analysis and simulation of the XANES spectra for our samples is described elsewhere Waychunas et al., (submitted).

1.3. Zn^{2+} Sorption in Related Systems

Schlegel et al. (1997) examined Zn sorbed on goethite and found distorted octahedral Zn complexes sharing both edges (Zn-Fe distances of 3.00 Å) and vertices (Zn-Fe distances of 3.20 Å) with surface Fe octahedral units. Both distances are consistent with those reported in our model compound survey and are indicative of octahedral–octahedral correlations with ES. For example, ES octahedra in the double octahedral chain structure of $Zn(OH)(NO_3) \cdot H_2O$ (Eriksson et al., 1989) have Zn-Zn distances of 3.09 and 3.26 Å. CS would seem to require longer distances than the reported 3.20 Å because Zn-O polyhedra are larger than Fe^{3+} polyhedra, and CS Fe^{3+} octahedra typically have Fe-Fe distances of 3.4 Å or more (Manceau and Combes, 1988). However, the concept of distorted zinc octahedra on the goethite surface are consistent with Gerth's (1990) observations assuming that there is solid solution formation.

More recently, Manceau et al. (2000a,b) studied trace-level Zn in natural and synthetic goethites via EXAFS, their analysis suggesting a solid solution with octahedrally coordinated Zn substituting for Fe^{3+}. However, their results show a first shell contraction with respect to the regular goethite structure, instead of the anticipated expansion as we indicated above. Zn sorption on alumina (mixed α and γ varieties) was examined by Trainor et al. (2000) via XAS methods. They found that at low surface coverages (below 1.1 mol/m², equivalent to ~0.03 Zn/Zn + Fe in the present study) that the Zn complexes were mainly tetrahedral with mean Zn-O bond length of 1.97 Å. At higher coverages, a hydrotalcite precipitate was formed, giving rise to specific multiple scattering effects in the EXAFS— namely, the appearance of a peak in the Fourier transform in the range of 4.5 to 6.5 Å due to Zn $\leftrightarrow$ Zn $\leftrightarrow$ Zn focused scattering. The tetrahedral complexes were assigned as ES with AlO_6 polyhedra with a Zn-Al distance of ~3.00 Å, though an undistorted arrangement would predict a distance of 2.6 Å. Hence, the polyhedra in this complex must be highly distorted.

Bochatay and Persson (2000) examined Zn sorption on manganite and found evidence for a Zn coordination change from mixed octahedral/tetrahedral to mainly tetrahedral with increasing pH and sorption density. The Zn formed either a multinuclear complex or a zinc hydroxide phase on the surface, and zinc hydroxide polymerization was inferred to occur at surface coverages above 1.1 mol/m².

Harvey and Linton (1984) studied Zn sorption on HFO via XPS with dried samples. They detected a change in Zn speciation with increasing pH and surface coverage, which was attributed to formation of a polymerized zinc hydroxide precipitate. This change occurred above pH 6.5 and at surface coverages of Zn equivalent to a Zn/(Fe + Zn) ratio above 0.12. With their HFO surface area, this corresponded to surface coverages of ~50% of a monolayer. This type of analysis does not directly reveal Zn coordination, although comparison with XPS reference spectra indicated that the precipitate was consistent with a tetrahedrally coordinated Zn compound. Harvey et al. (1983) observed a proton release of 1.73 for zinc adsorption on HFO under Langmuir conditions (Fig. 1), consistent with formation of two M-O bonds at the surface. This contrasted with Benjamin and Leckie (1981), who showed that at non-Langmuir conditions (Fig. 1) a proton release of 3.20 is observed during zinc sorption on HFO. This is consistent with multinuclear rearrangement such as from a different type of zinc surface complex, zinc polymerization on the surface, or HFO surface coordination changes.

To summarize these observations, Zn^{2+} appears generally to form isolated complexes on a variety of substrates at low coverages. The sorbing complex may be tetrahedral or octahedral. However, at higher coverages that are system dependent but generally well below monolayer density, precipitation occurs involving coordination changes and polymerization. The nature of these precipitates also varies with system parameters.

2. EXPERIMENTAL METHODOLOGY

2.1. Sample Preparation

Two-line ferrihydrite (FHY) was synthesized for adsorption samples following the method described in Waychunas et al.

Table 1. Zn-O and Zn-Zn,Fe distances in EXAFS model and structure reference compounds.[a]

Compound (mineral)	CN	(Å)	(Å)	Ratio 4/6 CN	Topology[b]
Zn_2SiO_4 (willemite)	4	1.955	3.197 T-T		Phenakite 3D[1]
ZnO (zincite)	4	1.978	3.230 T-T		Wurtzite 3D[2]
$ZnFe_2O_4$ (franklinite)	4	1.99	3.50 T-O		Spinel 3D[3]
			3.66 T-T		
$ZnCO_3$ (smithsonite)	6	2.1107	3.672 O-O		Calcite 3D[4]
$Zn_5(OH)_6(CO_3)_2$ (hydrozincite)				2/3	Bridged oct/tet layer[5]
	6	2.10	3.153 O-O		
	4	1.95	3.57 T-O		
			3.50 T-T		
$(Zn,Mg,Mn)_4Zn_3(CO_3)_2(OH)_{10}$ (sclarite)				3/4	Bridged oct/tet[6]
	6	2.127	3.168 O-O		Stepped layer
	4	1.950	3.563 T-O		
			3.665 T-T		
γ-Zn(OH)	4	1.96	3.458 T-T		Linked tet 3D[7]
α-Zn(OH)$_2$	6	2.13	3.14 O-O		ES oct layer[8]
ε-Zn(OH)$_2$ (wülfingite)	4	1.96	3.428 T-T		Linked tetrahedra 3D[9]
$Na_2Zn_2O_3$	4	1.98	3.430 T-T		Linked tetrahedra 3D[10]
γ-Zn$_3$(PO$_4$)$_2$	6	2.103	3.48 T-O	2/1	Linked oct/tet 3D[11]
	4*	2.04	2.98 T-T		
β-Zn$_3$(PO$_4$)$_2$	5	2.09			3D network[12]
	5	2.08			
	4	1.98			
$3Zn(OH)_2 \cdot ZnSO_4 \cdot 3H_2O$			3.152 O-O	1/3	Bridged oct/tet layer[13]
	6	2.14	3.520 T-O		
	4	1.93	3.493 T-T		
$Zn(OH)_2 \cdot ZnSO_4$	6	2.07	3.12 O-O		Chains of ES oct tied[14]
	4	2.01	3.39 T-O		by CS tet chains
			3.22 T-T		
$Zn_2Mo_3O_8$	6	2.14		1/1	Bridged MoO$_6$ layers[15]
	5	1.92	3.39 O-T		
α-ZnMoO$_4$	6	2.078			3D network[16]
	6	2.025			
$Zn_2(OH)PO_4$ (tarbuttite)[17]					
	5	2.041			
	6	2.025			
$(Zn_2Cu)_4SO_4(OH)_6 \cdot 4H_2O$ (namuwite)				1/3	Bridged oct/tet layer[18]
	6	2.14	3.175 O-O		
	4	1.95	3.554 T-O		
			3.524 T-T		
$Zn_2Cr(OH)_6X \cdot nH_2O$	6	NA	3.06 O-O		Oct layer[19]
$Zn_5(OH)_8(NO_3)_2 \cdot 2H_2O$				2/3	Bridged oct/tet layer[20]
	6	2.128	3.134 O-O		
	4	1.947	3.602 T-O		
			3.421 T-T		
$Zn(OH)NO_3 \cdot H_2O$	6	2.20	3.09, 3.26 O-O		ES oct double chains[21]
$Zn_5(OH)_8Cl_2 \cdot H_2O$ (simonkolleite)				2/3	Bridged oct/tet layer[22]
	6	2.165	3.17 O-O		
	4	2.02**	3.60 T-O		
			3.39 T-T		
$(Zn,Cu)_6Zn_2(OH)_{13}[(S,Si)(O,OH)_4]_2$ (bechererite)				2/3	Bridged oct/tet layer[23]
	6	2.122	3.195 O-O		
	4	1.923	3.578 T-O		
			3.766 T-T		
$Zn(H_2O)_6$ (aqueous)	6	2.11			
$Zn_2Cu(AsO_4)_2$ (stranskiite)[24]					
	5	2.06			
$Zn_2(OH)AsO_4$ (adamite)[25]					
	6	2.131	3.023 O-O		3D network
	5	2.024			

[a] Oct = octahedral; tet = tetrahedral; 3D = three-dimensional. * = ZnO$_4$ groups share edges. ** = average of 3 Zn-O bond lengths in ZnO$_3$Cl group.
[b] Numbers refer to the following references. 1. Klaska et al. (1978). 2. Kihara and Donnay (1985). 3. Hill et al. (1979). 4. Effenberger et al. (1981). 5. Ghose (1964). 6. Grice and Dunn (1989). 7. Christensen (1969). 8. Feitknecht (1938); see also Wegmüller (1987). 9. Schnering (1964). 10. Vielhaber and Hoppe (1965). 11. Calvo (1963). 12. Stephens and Calvo (1967). 13. Bear et al. (1986). 14. Iitaka et al. (1962). 15. Ansell and Katz (1966); McCarroll et al. (1957). 16. Abrahams (1967). 17. Cocco et al. (1966). 18. Groat (1996). 19. DeRoy et al. (1985). 20. Stählin and Oswald (1970). 21. Eriksson et al. (1989). 22. Allman (1968). 23. Giester and Rieck (1996). 24. Plieth and Sänger (1967). 25. Hawthorne (1976).
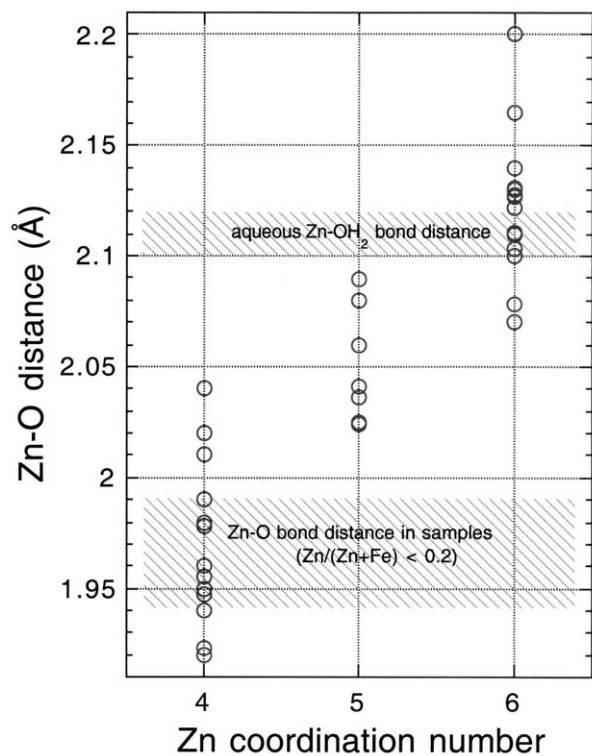
Fig. 3. Zn-O distance in samples and model compounds. Hatched areas indicate distances obtained in this study, including uncertainties.

Fig. 4. Zn-Zn distances in samples and model compounds. Hatched areas indicate distances obtained in this study, including uncertainties.

(1993) and Fuller et al. (1993). Samples were prepared in a sealed reaction vessel that was continuously purged with nitrogen during precipitation of ferrihydrite, addition of Zn, and concentration of the precipitate. A vessel was used that had inlet and outlet tubes for purging with nitrogen at a flow rate of 50 cm^3/min. The effectiveness of this technique was not tested; however, purging commenced while the system was acidic (pH < 4), where carbon dioxide is minimally soluble. Hence, CO_2 could only enter the system by invasion into the continuously pumped environment.

Ferrihydrite was prepared in a 0.1 mol/L $NaNO_3$ background electrolyte solution contained in a stirred, Teflon-lined reaction vessel purged with N_2. An acidified ferric nitrate solution (0.25 mol/L in 0.1% v/v HNO_3) was added to yield a total iron concentration of 10^{-3} M. The pH was then raised to 6.5 or 7.0, depending on the sample, to initiate Fe hydrolysis and precipitation by addition of CO_2-free 1 M NaOH with a syringe pump over a 10-min period. The resulting precipitate was aged for 24 h with the pH maintained with pH stat at 6.5 ± 0.1 or 7.0 ± 0.1. After the 24-h aging period, an acidified $Zn(NO_3)_2$ solution (0.05 mol/L) was added to yield the desired total Zn^{2+} concentration (10^{-5} to 10^{-3} M). After Zn addition, pH was adjusted by manual addition of 0.1 N NaOH and maintained to within 0.2 pH units throughout the equilibration period (1 to 21 d). Coprecipitated Zn-FHY samples were prepared following the method of Fuller et al. (1993). Acidified zinc and ferric nitrate solutions (2.5×10^{-3} to 0.25 mol/L Zn and 0.25 mol/L Fe) were metered (0.2 mL/min) into a stirred, Teflon-lined reaction vessel containing the background electrolyte by using a syringe pump fitted with two syringes. CO_2-free 1 N NaOH
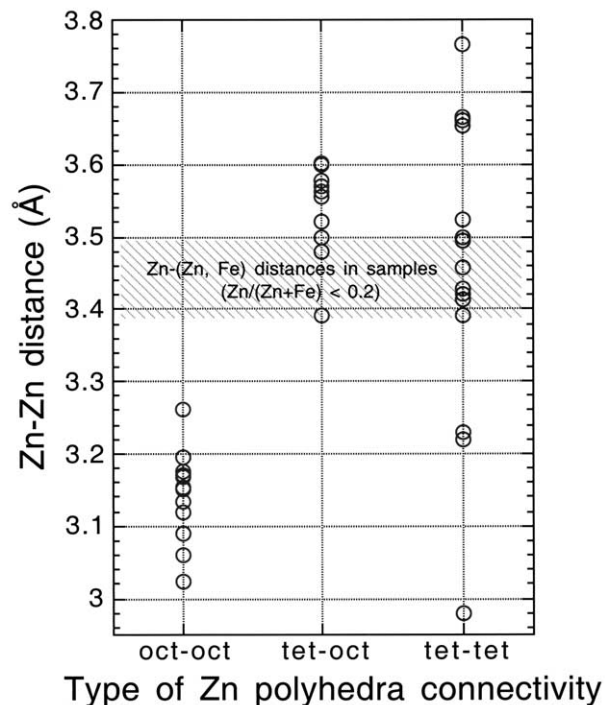
was added simultaneously with a second syringe pump to maintain the pH within 0.2 pH units throughout the metal addition, which required 20 min. The total Fe concentration was 10^{-3} M for all samples. Total Zn concentration ranged from 10^{-5} to 10^{-3} M. The resulting Zn-FHY system was aged for 2 to 7 d at constant pH by manual addition of 0.1 N NaOH. In one sample (4ZN-C6), the Zn and Fe solutions were added over a 4-h period. For both adsorption and coprecipitation samples, the final pH was measured and a sample of supernatant was collected for dissolved Zn^{2+} analysis. Dissolved Zn concentrations were measured by ICP-OES. The concentration of Zn uptake from solution was calculated from the difference between total Zn concentration and solution Zn concentration at the end of the equilibration period. The solid phase then was concentrated by settling and centrifugation for mounting in sample holders for XAS data collection.

A Zn sorption sample with greater adsorption density was prepared by incremental increases in the dissolved Zn concentration after an initial adsorption step. After the usual 24-h aging period, Zn was added to the ferrihydrite suspension to yield a total concentration of 10^{-3} M Zn. The system was equilibrated at pH 6.5 + 0.1 for 4 h. Subsequently, the total Zn concentration was increased 7.5-fold by incremental (5×10^{-4} M) additions of $Zn(NO_3)_2$ at 1-h intervals. A pH stat was used to maintain a constant pH throughout addition of Zn and subsequent equilibration. The resulting suspension was aged for 48 h at constant pH (6.5 + 0.1). Samples of the supernatant were retained for chemical analyses by the methods outlined above. The solid phase was concentrated for collection of XAS data. The Zn/(Zn + Fe) ratio of the solid was determined by acid dissolution of a portion of the precipitate and Zn, Fe, and

Table 2. Sample compositions and chemical analyses.[a]

SynID	Aging (d)	pH	Zn/(Zn + Fe)	Zn sorbed (%)	$[Zn^{2+}]$ solution
4ZnC5	7	7.00	0.007	62.6	3.97E-06
3ZnC2	7	6.02	0.020	ND	5.0E-05
4ZnC4	7	7.00	0.032	57.5	2.09E-05
4ZnC3	1	6.25	0.044	20.3	1.64E-04
6ZnC2	2	6.6	0.046	15.1	4.05E-04
3ZnC1	7	6.10	0.057	ND	2.0E-04
4ZnC1	21	6.45	0.070	34.6	1.33E-04
4ZnC2	7	6.30	0.078	13.7	4.89E-04
6ZnC1	3	6.5	0.088	7.4	9.27E-04
4ZnC6	7	6.85	0.128	67.6	6.97E-05
4ZnC7	7	6.40	0.130	13.8	8.96E-04
4ZnA4	7	6.75	0.004	36.2	6.50E-06
4ZnA3	7	6.50	0.018	31.9	3.45E-05
4ZnA2	7	6.20	0.028	13.1	1.76E-04
3ZnA2	7	6.07	0.029	ND	5.0E-05
4ZnA1	7	6.15	0.045	4.3	9.86E-04
6ZnA1	5	6.5	0.082	4.7	9.84E-04
6ZnA2	3	6.6	0.083	15.0	1.45E-04
3ZnA1	7	6.04	0.107	ND	2.0E-04
7ZnA1	1	6.5	0.50	11.9	5.9E-03
7ZnAmor1	See text		1.00	NA	See text
7ZnAmor2	See text		1.00	NA	See text
4ZnC3 supernatant		6.25	1.00		1.64E-04
6ZnG1	4	6.5	0.005	12.1	8.79E-04

[a] ND = not determined; NA = not applicable.

Na analysis by ICP-OES. The Zn/Na ratio in the supernatant and the Na concentration in the precipitate were used to correct the precipitate Zn concentration for entrained aqueous Zn. The entrained solution accounted for 2% of the Zn measured in the precipitate. Only about 10% of total Zn added was associated with the solid phase but yielded a Zn/(Zn + Fe) molar ratio of 0.5 for the solid. The total Zn concentration of 6.7×10^{-3} M was undersaturated with respect to $Zn(OH)_2$, $ZnCO_3$, and $Zn_5(OH)_4(CO_3)_2$ by factors of 135, 3, and 2 times, respectively, at pH 6.5, assuming equilibrium with atmospheric CO_2. The degree of saturation for carbonate phases likely was much lower because of the precautions taken to exclude CO_2.

Two synthetic zinc hydroxide phases were prepared for comparison to the adsorbed and coprecipitated samples. The first sample was prepared following the method of Schindler et al. (1964) for γ-$Zn(OH)_2$. The sample proved to exhibit only an amorphous-like diffraction pattern. A second zinc hydroxide was prepared by precipitation of a 0.5 M $Zn(NO_3)_2$ solution by addition of CO_2-free 1.0 N NaOH at 25°C (Dietrich and Johnston, 1927). A 200-mL solution of 0.5 mol/L $Zn(NO_3)_2$ was adjusted to pH 3 and purged with N_2 for 1 h in a stirred, Teflon-lined, water-jacketed glass reaction vessel. The pH of the zinc solution was increased to pH 6.5 by addition of CO_2-free 1.0 N NaOH with a syringe pump. The base addition was completed in 20 min. A white flocculent precipitate was visible at pH 6. The precipitate was aged for 24 h in the reaction vessel under nitrogen at constant pH (pH 6.5 + 0.1). The precipitate was concentrated by settling and subsequently washed three times with deionized water to remove dissolved nitrate from the system. The precipitate was concentrated by centrifugation after each wash as noted above. An X-ray diffraction scan showed only amorphous character for the precipitate. Chemical analyses for all samples are shown in Table 2.

2.2. EXAFS Procedures

EXAFS analysis was similar to that described in detail in Waychunas et al. (1993). We utilized an ion chamber–type fluorescence detector for most work (Stern and Heald, 1979); data were collected in both fluorescence and transmission modes simultaneously. A serious problem in Zn EXAFS work on iron oxides or oxyhydroxides is the strong absorption and attending fluorescence due to the iron matrix. This unwanted fluorescence signal swamps presently available multielement solid state detector arrays so that these are not effective in collecting EXAFS data for this system at low Zn concentrations. Another problem is the presence of glitches (i.e., double diffraction events) in the Zn EXAFS energy range on all of the Si (220) monochromator crystals available for Zn EXAFS work at Stanford Synchrotron Radiation Laboratory (SSRL). The glitches prevented data collection for samples with Zn/(Zn + Fe) ratio below 0.004 and required heroic efforts at spectra deglitching in this compositional range. Si (111) monochromator crystals were less problematic for EXAFS but yielded insufficient energy resolution for near-edge studies. Hence, considerable repeat analysis was performed with freshly made analogous samples to collect sufficient quality near-edge and EXAFS data.

Data was collected on SSRL wiggler beam lines 4-1, 4-3, and bending magnet beam line 2-3. Line 2-3 was used mainly for model compound and standard analyses. Monochromator detuning based on I_0 set at the center of the scan range was 30% for (111) silicon crystals and 60% for (220) monochromator crystals. Samples were both of wet and dry preparations, and these were handled as described in Waychunas et al. (1993). EXAFS modeling was accomplished with the SSRL routines Process and Opt (George and Pickering, 1995) with simulated spectra, phase-shift functions, and amplitude functions calcu-

Table 3. EXAFS results Zn K edge and Fe K edge.[a]

SynID	Zn-O first shell				Zn-Zn,Fe second shell			
	CN	R/Å	DW/Å^2	ΔE_0/eV	CN	R/Å	DW/Å^2	ΔE_0/eV
4ZnC5	4.05	1.98	0.006	1.2	4.0	3.42	0.012	1.2
3ZnC2	4.45	1.96	0.007	1.65	2.5	3.42	0.012	1.65
4ZnC4	4.25	1.94	0.007	1.25	1.7	3.38	0.010	1.25
4ZnC3	4.31	1.95	0.008	1.06	1.50	3.41	0.010	1.06
6ZnC2	3.93	1.96	0.007	0.56	1.2	3.48	0.011	0.56
3ZnC1	4.36	1.95	0.007	−2.45	1.61	3.44	0.010	−2.45
4ZnC1	4.34	1.97	0.007	1.8	1.8	3.43	0.008	1.8
4ZnC2	4.15	1.96	0.008	1.2	0.93	3.38	0.010	1.2
6ZnC1	4.23	1.98	0.008	−1.1	0.90	3.40	0.011	−1.1
4ZnC6	3.79	1.98	0.008	1.44	1.1	3.45	0.016	1.44
4ZnC7	3.68	2.00	0.008	1.90	0.9	3.47	0.009	1.90
4ZnA4	5.05	1.96	0.007	1.2	1.93	3.43	0.012	1.2
4ZnA3	4.21	1.95	0.008	−0.50	1.29	3.50	0.013	−0.50
4ZnA2	4.12	1.96	0.008	0.63	1.30	3.41	0.012	0.63
3ZnA2	4.07	1.97	0.008	−0.82	1.35	3.43	0.010	−0.82
4ZnA1	3.79	2.01	0.008	0.45	1.2	3.50	0.012	0.45
6ZnA1	4.02	1.97	0.007	−1.5	0.76	3.50	0.010	−1.5
6ZnA2	4.20	1.97	0.008	−0.3	0.74	3.47	0.010	−0.3
3ZnA1	4.28	1.96	0.008	−1.5	0.64	3.45	0.010	−1.5
7ZnA1	4.95	1.99	0.010	1.4	1.2	3.10	0.011	1.4
7ZnAmor1	6.05	2.04	0.008	1.8	2.0	3.11	0.008	1.8
					1.6	3.62	0.008	
7ZnAmor2	5.37	2.04	0.008	2.1	4.4	3.13	0.010	2.1
					2.5	3.57	0.010	
4ZnC3 supernatant								
	6.8	2.13	0.011	1.4				
10^{-3}M ZnNO$_3$	6.3	2.12	0.009	−0.33				
Franklinite	4.20	1.97	0.0065	2.9	11	3.51	0.006	2.9
Smithsonite	6.05	2.108	0.009	1.00				
Hydrozincite	5.4	2.04	0.014	2.5				
Ferrihydrite	5.8	2.00	0.008	1.5	5.5	3.04	0.012	1.5
					3.5	3.45	0.012	
3ZnA1	5.8	2.00	0.009	0.36	5.24	3.06	0.016	3.5
					3.26	3.44	0.016	
ZnCl	6.2	2.01	0.010	0.63	4.89	3.05	0.016	4.1
					2.57	3.42	0.016	
4ZnC9	5.5	2.01	0.008	−0.77	4.43	3.05	0.016	2.2
					1.98	3.42	0.016	

[a] CN = coordination number; R = interatomic distance; DW = Debye-Waller factor.

lated by Feff 7.0 (Ankudinov et al., 1996; Ankudinov and Rehr, 1997) and Feff 8.0 (Ankudinov et al., 1998). Both standard EXAFS and multiple scattering effects (Rehr et al., 1992) were calculated for a range of cluster types. Model compounds used in testing and data analysis included franklinite (tetrahedral Zn, octahedral Fe^{3+}), zincite (tetrahedral Zn), willemite (tetrahedral Zn), smithsonite (octahedral Zn), hematite (octahedral Fe^{3+}), and hydrozincite (tetrahedral and octahedral Zn). Uncertainties in fitting parameters are calculated by Opt by using fits to unfiltered full EXAFS spectra. In general, these uncertainties underestimate parameter error because they do not include systematic effects produced by anharmonicity, nonconstant amplitude reduction factor S_0^2, and incorrect choice of E_0. Hence, in the present work, we use commonly accepted uncertainties of 2% for bond distances and 15% for coordination numbers, except when the Opt fits yield larger values. E_0 values were taken to be the energy at the mid height of the leading part of the edge. Delta E_0 values relative to this are noted in the fitting results in Table 3. S_0^2 values varied among models between 0.85 and 0.90 for the Zn K edge, and 0.87 was used for

sample fitting. Monochromator energy calibration was performed with separate Fe and Zn metal foils run at intervals among the other data scans. Use of a Zn foil between a second and third ion chamber for continuous calibration was found to contaminate the transmission signal recorded by the second chamber; it also scattered into the sample region. Hence, this mode of calibration was not used.

3. RESULTS

3.1. EXAFS Analysis of Zn Edge

3.1.1. Coprecipitation and Adsorption Samples

Raw K-edge Zn X-ray absorption spectra for a representative set of samples and for a 0.001 M aqueous Zn nitrate solution are shown in Figure 5. The spectra appear to change continuously as a function of Zn content, with a significant loss of high-frequency components with initial increase in Zn, then a change to a different EXAFS (and XANES) pattern with Zn composing more than 50% of the sample. The extracted EX-
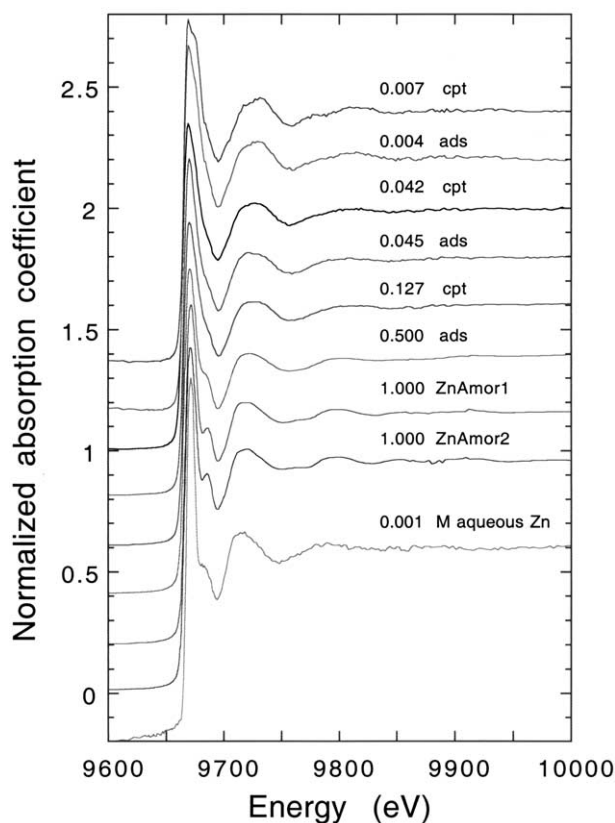
Fig. 5. Comparison of raw Zn K edge EXAFS spectra for suite of synthetic samples. Ads = absorption samples; cpt = coprecipitate samples.

Fig. 6. Extracted EXAFS functions for representative sorption samples.

AFS and radial structure functions (RSFs) shown in Figures 6 and 7, and 8 and 9, respectively, illustrate this more clearly. There appears to be no significant difference between the kind of spectrum or RSF seen for the coprecipitation and adsorption samples in the 0.004 to 0.127 Zn/(Fe + Zn) composition range except for the decrease in the higher-frequency component (and thus second shell RSF peak area). Comparison of the sample RSFs with model compounds (Fig. 10) illustrates the distinctive similarities. The best agreement is with the franklinite RSF, where the first and second shell peaks occur at essentially the same distances as in the ferrihydrite samples. This is a characteristic tetrahedral distance for the Zn-O shell first peak, and a characteristic tetrahedral–tetrahedral or octahedral–tetrahedral distance for the Zn-Fe,Zn shell second peak (Figs. 3 and 4, respectively). However, the distance for the second shell in the RSF is not necessarily always distinctive, as can be seen in the hydrozincite model RSF. In hydrozincite, there are significant octahedral–octahedral Zn-Zn correlations, yet the second shell peak distance does not obviously reflect this. Because the simulated hydrozincite RSF established by a Feff 7.0 calculation of the EXAFS yields good agreement, this demonstrates that direct comparison of EXAFS-derived RSF second shell peak positions between models and samples must be made with caution. This is because of the other possible contributions to this second shell peak (mainly Zn-O) and complex second shell distance distributions that can affect the overall EXAFS amplitudes.
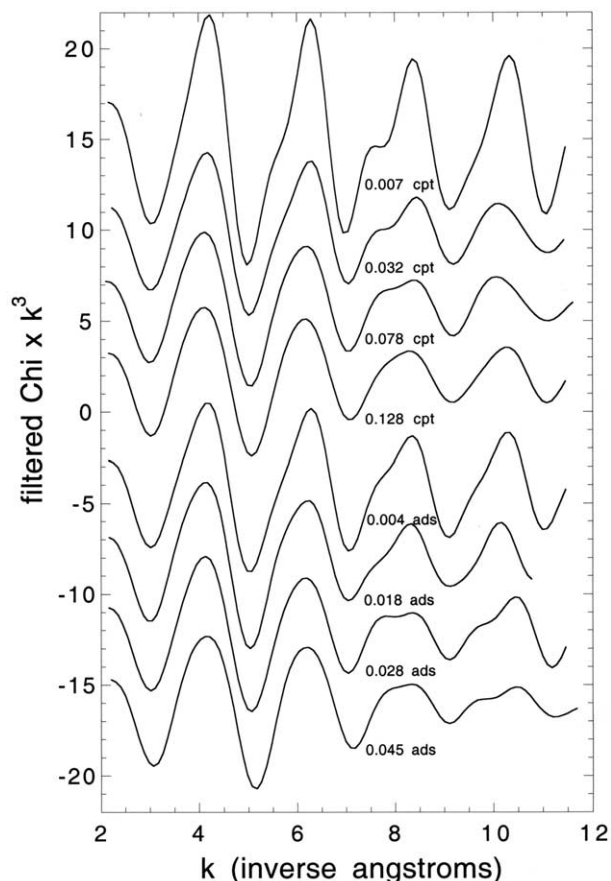
Fitting was performed in k-space and r-space for different combinations of first shell Zn-O distances and second shell Zn-Zn,O,Fe distances. Our usual procedure was used: we fitted filtered data from each shell separately, then used these results to directly fit the raw EXAFS spectra. Although two first shell Zn-O distances could always be fit to the first RSF peak, fit quality was not improved so markedly that these distances could be used for structural interpretation without ambiguity. Hence, we used first shell average Zn-O distances for comparison with the values shown in Table 1. Representative fits for the full EXAFS are shown in Figure 11 for both r-space and k-space. The Zn-O distances (Fig. 12) were found to be constant for all coprecipitation and adsorption samples at 1.965(15) Å. This distance is consistent with the overall average Zn-O distance calculated from tetrahedral sites in the structures listed in Table 1, and is about 0.14 Å smaller than the corresponding average octahedral Zn-O distance. We were also able to determine accurate average Zn-O distances for the model compounds examined (Table 3). For the hydrozincite model, with three kinds of Zn sites and a large range of Zn-O distances, this result indicated that nongaussian bond length distributions should not greatly affect the fitted Zn-O distances for our experimental samples—that is, the correct average Zn-O distance was obtained despite the complex distribution. Zn-O first shell coordination numbers varied slightly over the compositional range 0.004 to 0.127 Zn/(Zn + Fe), with a least-squares
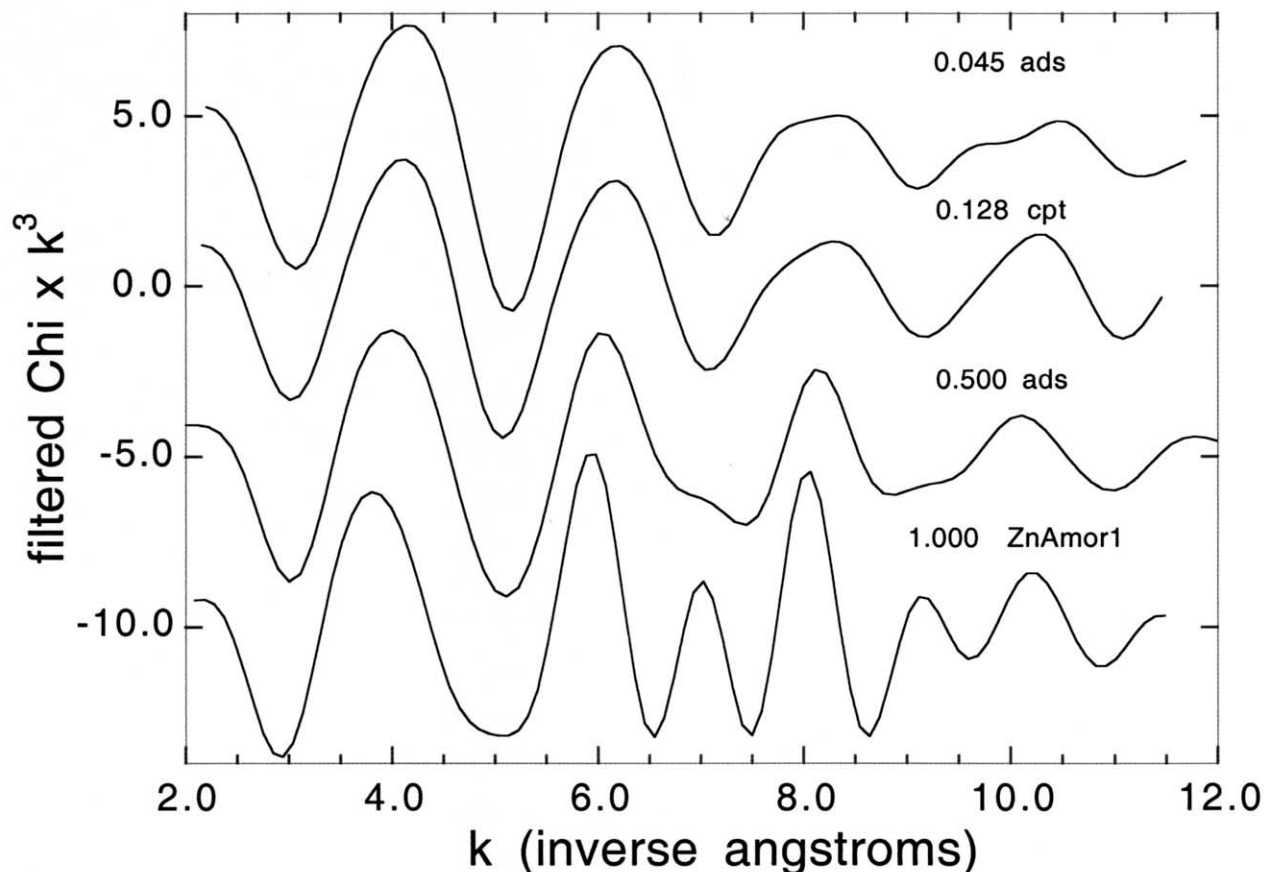
Fig. 7. Extracted EXAFS functions for high Zn-loaded samples compared with sorption samples.

fit (Fig. 13) being affected by the lowest Zn composition point. Accepting the fitted trend as indicative of the samples as a whole yields a variation of coordination number from 4.4 to 4.0 oxygens, which would be consistent with a mixture of octahedral and tetrahedral Zn sites changing from 80 to 100% tetrahedral with increasing Zn content. To compare this with the first shell model compound Zn-O distances, by using the average values from Table 1 for octahedral and tetrahedral Zn-O distances, the 0.02 Å uncertainty in Zn-O distances from the fitting would allow a maximum of 15% octahedral Zn-O component. Hence, the combination of both results allows for at most a small fraction of octahedral Zn at the lowest Zn contents.

The second shell of the RSFs was fit by a range of models to determine if this contribution was due to Zn-Fe, Zn-Zn, or Zn-O correlations. A solely Zn-O contribution could not fit the filtered EXAFS and was completely out of phase with the k-space oscillations. However, Zn-Fe and Zn-Zn contributions fit the EXAFS oscillations about equally well with a small systematic effect on Zn-X distance and coordination number. Because we observe mainly tetrahedral Zn-O sites, the presence of Zn-Zn correlations would imply CS or ES ZnO_4 tetrahedra. On the other hand, Zn-Fe correlations imply ZnO_4 attachment to FeO_6 octahedra by CS or ES because there is no convincing evidence for significant tetrahedral Fe^{3+} in any form of ferrihydrite (Waychunas et al., 1996). Within the fit uncertainty

(0.06 Å) the Zn-Fe,Zn distance did not vary as a function of sample composition (Fig. 12). Allowing for structural changes caused by variations in hydrogen bonding about an aqueous complex, this distance is consistent with ZnO_4-FeO_6 CS sites in franklinite and ZnO_4-ZnO_4 CS sites in γ-$Zn(OH)_2$ and ε-$Zn(OH)_2$, as well as ZnO_4-ZnO_6 CS sites in hydrozincite and several of the brucite-like layer structures. The absence of substantial octahedral Zn rules out the hydrozincite-like contribution, but the other linkages remain possible.

Second shell coordination numbers vary as a function of total Zn composition, which may be considered as surface Zn density on the adsorption samples (Fig. 13). The coordination varies from 4.0 to less than 1.0 for the coprecipitation samples, and from 2.0 to less than 0.7 for the adsorption samples. At the low end of these ranges, the coordination numbers are relatively more uncertain because the amplitude of the second shell is not much larger than other ripples in the Fourier transform. The variation in coordination number was tested with several models: addition of other EXAFS contributions at other distances creating interfering oscillations; addition of gaussian (harmonic) disorder; and addition of nongaussian (anharmonic) disorder. No reasonable single new Zn-Fe or Zn-Zn contribution (i.e., distances observed in a Zn-Fe model compound) reduced the second shell amplitude as observed. We were able to produce interference effects that reduced coordination number by adding Zn-O contributions at arbitrary distances, but
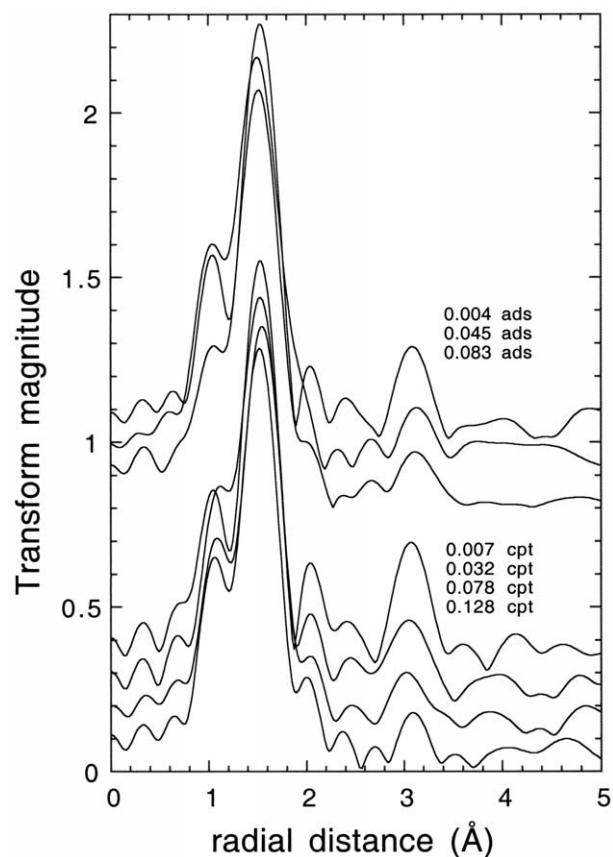
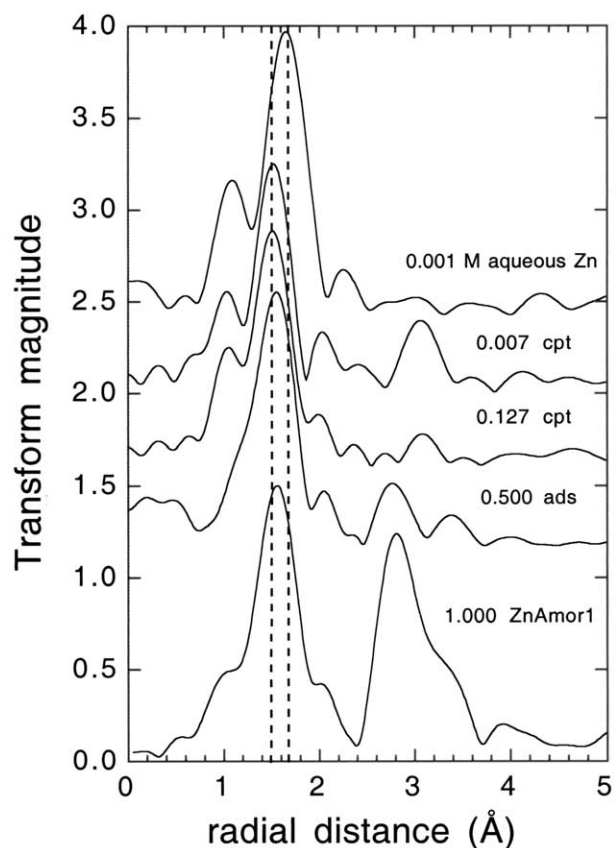Fig. 8. Experimental EXAFS RSFs for representative sorption samples

Fig. 9. Experimental EXAFS RSFs for sorption samples compared with aqueous Zn and high Zn loaded synthetics. Dashed lines indicate nominal positions for tetrahedral and octahedral Zn-O bond distances.

these were required to have substantially more amplitude than we would expect even in the most densely packed clusters, were not justifiable on crystal chemical grounds, and caused unusually poor fitting at low k values. Addition of gaussian disorder reduced the amplitude of the second shell, but this did not coincide with the form of the filtered second shell EXAFS contribution; that is, a Debye-Waller variation did not mimic the changes seen. However, addition of significant nongaussian disorder reduced the fitted coordination number without markedly affecting the fitted Debye-Waller (gaussian) factor. Addition of nongaussian distance distributions also showed that reduction in apparent second shell coordination number could occur along with mean second shell interatomic distance contraction. To place limits on how important these effect could be, we attempted to find a nongaussian Zn-Fe distribution that would account for the fitted coordination number for the highest Zn sorption levels but with no actual coordination number change from the dilute Zn samples. This was unsuccessful; it predicted large interatomic distance contractions that are not observed. The model that best effected the coordination change was the simple addition of Zn-Zn,Fe contributions having reduced coordination numbers and similar distances, such that the mean coordination number was reduced with increasing Zn composition. This could explain a drop in second neighbor coordination from 4.0 to about 1.3, but not to a smaller value. Several samples were produced with differing aging periods to see if this would affect the state of the Zn sorption complexes

(Table 2),—that is, 4ZnC1, 4ZnC2, and 4ZnC3 among others. Although it was not possible to achieve equal sorption densities on these samples and thus to completely separate out coverage effects, there appears no significant effect on the Zn XAS spectra as a function of aging up to 3 weeks.

3.1.2. High Zn Samples

The additional samples prepared to study the effect of higher Zn concentrations showed dramatic variations in the EXAFS compared with the lower Zn samples. The first shell Zn-O mean distance increased in the $Zn/(Zn + Fe) = 0.5$ sample to 2.00 Å, and to 2.04 Å in the amorphous Zn hydroxide samples. These changes are small but consistent with increasing octahedral Zn. For comparison, the mean Zn-O distance for hydrozincite is about 2.04 Å, with 60% of Zn sites octahedral. Unfortunately, multiple Zn-O first shell distances could not be fit meaningfully to the EXAFS given the distance resolution conferred from our k-space range ($\Delta k = 9$) of ~0.17 Å. All fit results are shown in Table 3. The second shell distance results are plotted as a function of composition in Figure 12. Coordination numbers are similarly plotted in Figure 13. More dramatic are the changes observed in the second shell, which becomes two separate contributions at ~3.15 and 3.56 Å, both of which can be fit with either Zn-Zn or Zn-Fe phase/amplitude factors, but not with Zn-O parameters. The contributions are small in the
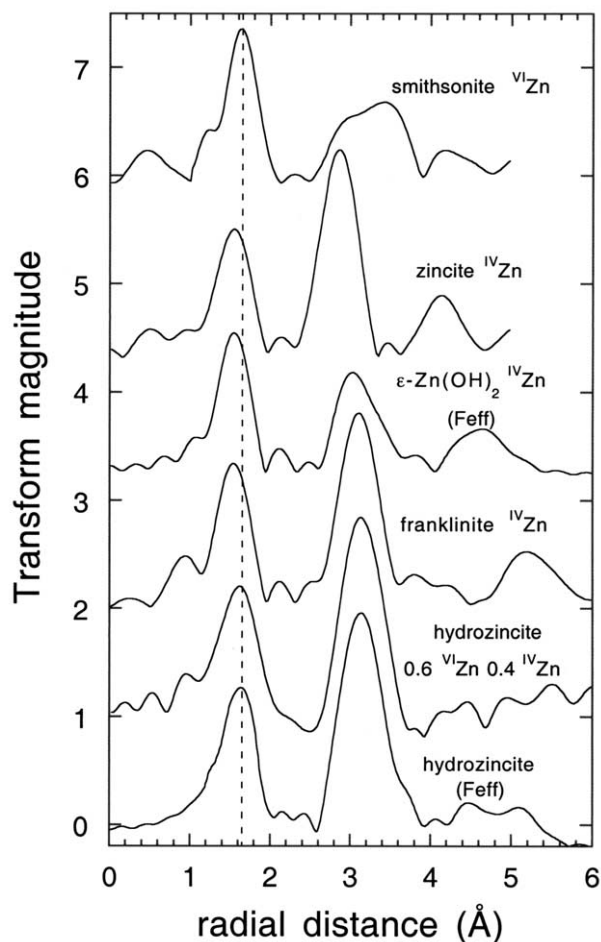
Fig. 10. Experimental and simulated EXAFS RSFs for Zn model structures. Dashed line indicates nominal octahedral Zn-O bond distance.

$Zn/(Zn + Fe) = 0.5$ sample, but increase greatly in the amorphous Zn hydroxide samples with little change in Zn-Zn,Fe distance. Comparison with the values in Table 1 suggests that the shift in Zn-O average distance and the 3.15 Å contribution are consistent with ES octahedral Zn groups. The 3.56 Å contribution is less clear and could be due to either ZnO_4-ZnO_6 CS or possibly ZnO_4-ZnO_4 CS linkages. Linkages with Fe polyhedra appear less likely, given the appearance of similar contributions in the synthetic zinc hydroxides with no Fe present. Another consideration is the ratio of the fitted coordination numbers for these two samples. The ratio of shorter to longer Zn-Zn distances can be seen from Table 1 to be an indication of the structural topology of the cluster or precipitate. For example, the layers in namuwite (structure XVI in Fig. 2) have six filled octahedral Zn sites per pair of tetrahedral Zn sites (on top and bottom of an octahedral Zn vacancy site). This yields average Zn second neighbor correlations of 3.75 octahedral–octahedral sites, 3.00 octahedral–tetrahedral sites, and 0.25 tetrahedral–tetrahedral sites. By assigning these to longer or shorter distances, a ratio of 3.75 short/3.25 long, or 1.15, results. For other structures, the ratios are smaller because of increased structural tetrahedral zinc occupying vacancies in an

otherwise planar or stepped octahedral Zn layer. In contrast, small octahedral sheets of Zn sites (brucite or α-$Zn(OH)_2$ structure) with sorbed tetrahedral Zn at their edges yield much larger ratios, depending on size. The high Zn samples we prepared yield ratios of 3.0(1.0) (7ZnA1) and 1.3 to 1.8(0.8) (7ZnAmor1, 7ZnAmor2), with the ratio much smaller in the pure Zn samples. Although the uncertainty in the ratios keeps us from assigning significant structural differences from these values, the overall large ratios suggest that an octahedral structure with mainly edge tetrahedral Zn is the most likely form for the initial precipitate. If a decrease in ratio does occur with increasing Zn content, this would indicate that at higher Zn concentration the paired tetrahedral/octahedral vacancy site is a favored structural motif. Fits to the EXAFS of these samples are shown in Figure 11.

3.2. Fe EXAFS

Most of the Fe XAS spectra and Fourier transforms of our samples showed little variations. However, small differences were detected in the coprecipitation samples with highest Zn content. A representative set of results are shown in Figure 14. The uppermost RSF is from a ferrihydrite sample prepared at pH 8 and aged for 1 d in its solution. This RSF is typical of the RSF seen for most of our ferrihydrites prepared with Zn. Sorption sample 3ZnA1, with $Zn/(Zn + Fe) = 0.107$ and one of the highest sorption densities, has a RSF that is essentially equivalent to that from samples with no sorbed Zn. Coprecipitation sample 3ZnC1, with $Zn/(Zn + Fe) = 0.056$, shows a second shell region that is slightly smaller than that from 3ZnA1. Coprecipitation sample 4ZnC7, with $Zn/(Zn + Fe) = 0.130$, shows additional reduction in the second shell region. Fitting results are shown in Figure 14. The change in second shell contributions can be seen by the decrease in intensity of the features at $k = 7.5$ and $k = 10.7$, and increase of the feature at $k = 9.7$ as Zn is added to the system via coprecipitation. Fitted first shell distances, coordination numbers and Debye-Waller parameters showed no statistically significant differences among these samples. However, fitting of the back-transformed EXAFS from the second shell reveals small changes. The total number of fitted Fe-Fe neighbors (Table 3) for 3ZnA1, 3ZnC1, and 4ZnC7 are 8.50 (.50), 7.46(.50), and 6.41(.63), respectively, for partially constrained fits of similar quality. This compares with the fitted numbers of Fe-Fe neighbors in ferrihydrite samples of similar age with no Zn that average ~8.2 with similarly constrained fits. The overall reduction of second shell coordination in the coprecipitation samples is three or more times the uncertainty and thus is certainly significant. Variations in the separate fitted Fe-Fe correlations also show that the change in the longer Fe-Fe neighbors is larger. These distances are due to CS of Fe octahedral units (Manceau and Combes, 1988), and reduction implies reduced polymerization of the precipitate.

These reductions in the second shell can be due to increases in disorder within the coprecipitated ferrihydrite, to ferrihydrite particle size reduction by surface poisoning, or to interferences in the EXAFS from Zn replacing Fe in structural positions— that is, from Zn-Zn and Zn-Fe backscattering phase cancellation. As shown earlier, the changes observed in the Zn-Fe,Zn RSF peak from the Zn EXAFS analyses were more dramatic in
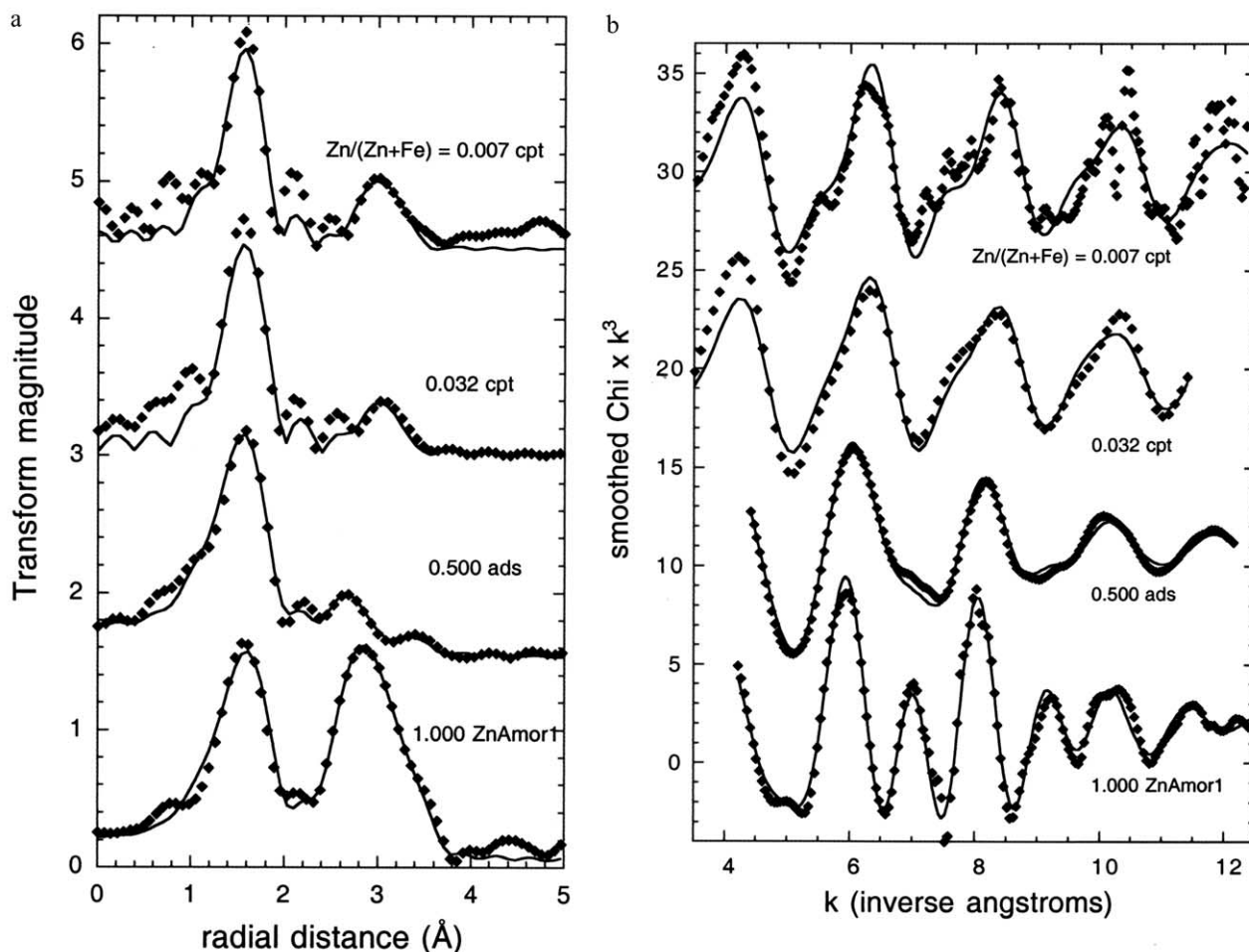
Fig. 11. (a) Representative least-squares fits to Fourier-transformed Zn EXAFS. Solid line is the calculated fit. (b) Least-squares fits to the unfiltered EXAFS spectra. Solid line is the calculated fit.

the coprecipitated samples. The fact that the effect of sorbed Zn is not obvious in adsorption samples, suggests that the sorbed Zn^{2+} is localized on the ferrihydrite surface, so that the average Fe "sees" only a very small proportion of the Zn population. In comparison, the coprecipitated Zn^{2+} has a large enough effect so that it can be considered quantitatively, which we do below.

4. DISCUSSION

4.1. Solid Solution Formation

The formation of ferrihydrite with Zn^{2+} randomly substituting for Fe^{3+} in the structure requires a substitution of OH^- for O^{2-}, i.e., $Zn^{2+} + OH^- = Fe^{3+} + O^{2-}$ or, alternatively, substitution of water for a hydroxyl, i.e., $Zn^{2+} + OH_2 = Fe^{3+} + OH^-$. In either case, the first coordination shell will have slightly lower formal charge, and this should lead to a mean increase in the metal–oxygen distance. An additional consideration is the average M-O bond length of octahedrally coordinated Fe^{3+} vs. Zn^{2+}. From past bond length analyses (e.g., Shannon and Prewitt, 1969) and known Fe oxide mineral structures (Waychunas, 1991), Fe^{3+}-O^{2-} and Zn^{2+}-O^{2-} distances for octahedral coordination differ by about 0.1 Å, with

Zn-O being longer. The exchange of hydroxyl for oxide extends each of these distances by about 0.1 Å. Hence, a change in metal ion from Fe^{3+} to Zn^{2+} and one hydroxyl or water ion replacement would be expected to increase the mean interatomic distance by $0.1 + 0.1/6 = 0.116$ Å. We would also expect some disorder to be visible in the various shells owing to more irregular O positions throughout the structure. Finally, there could also be a slight increase in the mean Fe-O distance due to the effects of additional water or hydroxyl in the structure. None of these predictions appear in the fitting results for the coprecipitation samples, indicating that a solid solution is not occurring or too few ions are involved to be detectable. As a separate issue, the strain induced by this substitution could be destabilizing. In general, Zn substitutions into planar octahedral Fe^{3+} structures appear limited.

In work that bears on this issue, Gerth (1990) synthesized goethite crystallites with varying amounts of dissolved metal ions including Zn. A linear relationship in the goethite cell dimensions was observed up to a Zn/(Zn + Fe) ratio of 0.06, suggesting solid solution formation. However, the octahedral ionic radius of Zn^{2+} was inconsistent with changes observed in the a-dimension, which required a distance closer to the tetra-
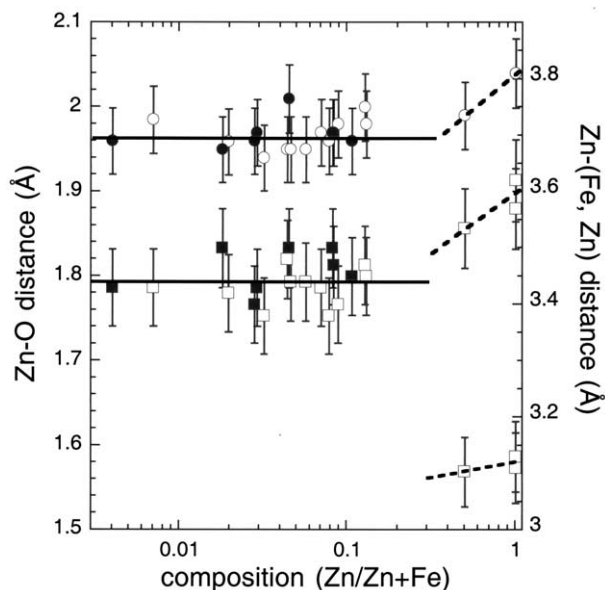
Fig. 12. Zn-O and Zn-(Zn,Fe) distances vs. composition from EXAFS fitting. Open circles and squares = coprecipitate samples; solid circles and squares = adsorption samples. Squares = second shell distances; circles = first shell distances.
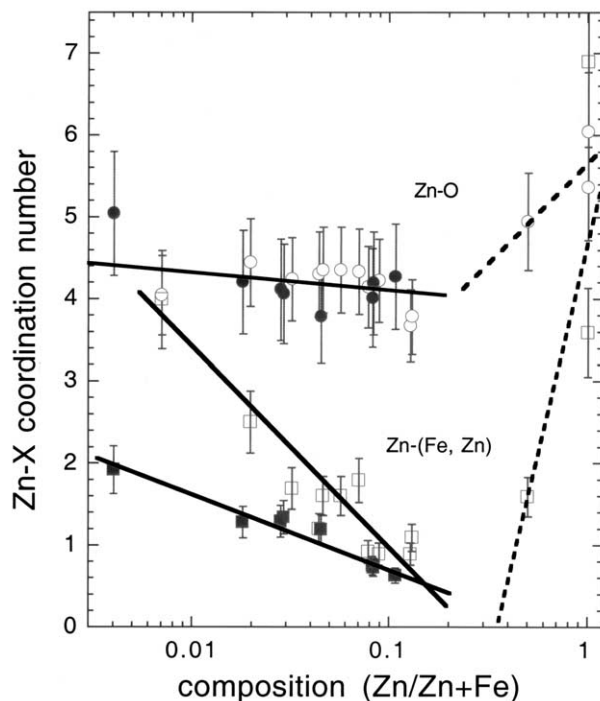

Fig. 13. Zn-X coordination numbers vs. composition from EXAFS fitting. Open circles and squares = coprecipitate samples; solid circles and squares = adsorption samples. Squares = second shell distances; circles = first shell distances.

hedral Zn^{2+} radius to achieve a linear relationship with composition. Schulze (1984) has shown that the goethite a-dimension is not a reliable indicator for metal substitution because of OH substitution and variations created by different synthesis conditions. On the other hand, linear relationships for the b-dimension were consistent with octahedral Zn^{2+} ion radii. Gerth (1990) suggested that Zn resided in the goethite structure within a distorted octahedron with Zn-O bond lengths as disparate as the octahedral/tetrahedral radii would suggest, or about 1.96 to 2.11 Å based on Shannon and Prewitt (1969) oxide radii. There is precedent for highly distorted octahedral Zn^{2+} sites—for example, within the octahedral Zn sites in $Zn(OH)_2 \cdot ZnSO_4$ (Iitaka et al., 1962) where the range of distances is 2.20 to 1.93 Å, but with an average distance of 2.07 Å. By use of our analysis above, a mean Zn-O distance of about 2.035 Å would be expected for a ZnO_6 octahedron in HFO, significantly different from our fitted result near 1.965 Å. A more distorted octahedron could create anharmonic effects that would lower the apparent coordination number. However, a more spread out distribution of Zn-O distances would be identifiable as well, and most highly distorted Zn coordination polyhedra occur in sulfates and nitrates. Gerth's (1990) samples were prepared under highly alkaline conditions that could possibly stabilize the substitution of OH^- for O^{2-}, or perhaps aqueous tetrahedral Zn^{2+}, so that a defect solid solution could have been produced.

Possible defect solid solutions are suggested by the known Zn crystal chemistry—for example, the formation of octahedral vacancies within octahedral layers topped with one or two tetrahedral Zn complexes (see structural model XVII in Fig. 2) and local spinel-cluster motifs. This topology in the former case is supported by the stability of the zinc layer structures, where bond valence sums at oxygens coordinated to the tetrahedral zinc ions (and to two octahedral Zn ions) would be equal to

$2/6 + 2/6 + 2/4 = 1.17$. Protonation of this oxygen would typically add about 0.83 bond valence units (with the rest given up to hydrogen bond formation; Brown, 1981) so that the sum would be perfectly 2.00. The bond valence sum for a planar FeO_6 structure with similarly bound tetrahedral zinc would be $3/6 + 3/6 + 2/4 = 1.5$, resulting in significant underbonding without protonation, and significant overbonding with protonation. This difference may in part explain why mixed $Zn-Fe^{3+}$ planar structures do not occur. Besides the bond valence problem, such a defect solution would also require us to detect larger Zn-Fe coordinations (i.e., six) than we observe. In spinels such as franklinite, the tetrahedral zinc ion shares all vertices with octahedral units. This gives three shared octahedral Fe^{3+} and one tetrahedral Zn^{2+} at an oxygen vertex, with a bond valence of $3/6 + 3/6 + 3/6 + 2/4 = 2.00$ for perfect bond valence satisfaction. Oxygens at such a defect are unprotonated, and thus this type of solution formation would be favored at high pH conditions, if at all. However, zinc is 12-fold coordinated by second neighbor iron in franklinite, so that this cannot match our observations, unless a smaller unit is required because of the topology of the ferrihydrite structure.

4.2. Surface Zn^{2+} Complex Geometry

Our results suggest a series of changing complexation/precipitation modes as a function of aqueous Zn concentration and type of preparation. How can these results be reconciled into the broader picture of complexation indicated by past work? As shown in Figure 1, the linear part (Langmuir region) of the isotherm was unreachable during our experi-
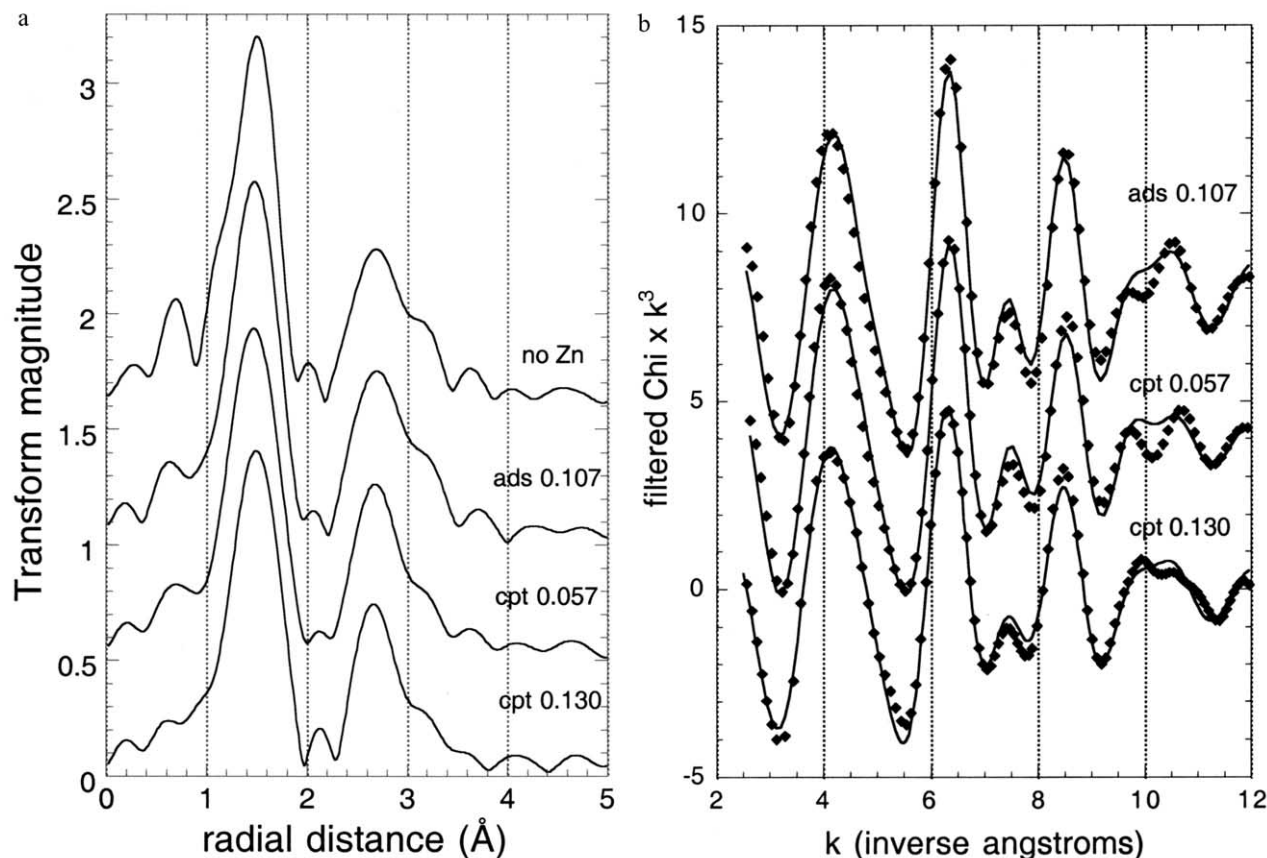
Fig. 14. (a) Fe K-edge RSFs for representative sorption samples. (b) Least-squares fits to Fe K-edge EXAFS samples. Diamonds = filtered data; solid lines = least-squares fit.

ments but may be consistent with aqueous $Zn\ (H_2O)_6$ surface complexation. Our lowest Zn sorption sample showed an increased nearest neighbor coordination, which suggests a small amount of six coordination Zn species, although within the uncertainties of the analysis, especially considering entrainment of aqueous Zn^{2+} solution. Could this type of complexation be stable on the HFO surface? A simple bond valence analysis at the surface of a HFO cluster composed of ES $Fe^{3+}O_6$ units is shown in Figure 15. Bonding of an octahedral zinc aqueous complex on the surface is clearly possible as 2/6 + 3/6 contributions from the Zn and Fe, respectively, plus a proton, yield a bond valence of ~1.66 to 1.83, depending on the degree of hydrogen bonding. However, a change of Zn coordination to tetrahedral would increase the oxygen bond valence sum to ~1.82 to 2.00 and thus would be favored. Theoretical calculations by Pavlov et al. (1998) suggest that the energy difference between 4- and 6- aquacoordinated Zn^{2+} ions are small. Within solids where Zn^{2+} has the option of filling either tetrahedral or octahedral sites (e.g., loseyite [Hill, 1981] and sclarite) there appears to be a definite preference for the tetrahedral site (Grice and Dunn, 1989). These results and observations suggest that relatively small changes in bond valence could have substantial effects on surface complex coordination changes.

Within the range of Zn/(Zn + Fe) from 0.004 to 0.127, our samples clearly indicate a tetrahedral Zn bonded to one to four

Zn or Fe ions. Because no tetrahedral ions are proven to exist in the HFO structure, the only possibilities are tetrahedral Zn–octahedral Fe, tetrahedral Zn–octahedral Zn, and tetrahedral Zn–tetrahedral Zn. All of these correlations have distances in known structures roughly consistent with our EXAFS results. For the lower Zn end of the range, it would be difficult to have Zn-Zn complexation unless there was formation of a surface precipitate. We have already discussed above why octahedral Zn substituting into HFO is unlikely to any large extent. Thus, for the lowest Zn samples, the best alternative is a tetrahedral Zn–octahedral Fe complex of the type shown in Figure 2 (structures IV, V, and VI). This type of complex explains the difference between the coprecipitated and adsorption samples. The coprecipitation case has sufficient aqueous Fe^{3+} available to form multiple bonds with tetrahedral Zn^{2+}, whereas the adsorption case only allows formation of surface bidentate bonds. But why, then, do we not see higher second-neighbor coordination numbers, as in the franklinite structure (Zn-Fe_{12})? One answer is that nonplanar FeO_6 polyhedra can be involved in the complexation in a double bidentate arrangement (Fig. 2, IV). This motif might be favored in coprecipitation processes over franklinite-type units, which may require growth to a larger size before reaching thermodynamic stability. Another possibility are the effects of formation of tetrahedral Zn–tetrahedral Zn polymers in solution near the surface or onto an already attached surface complex (structures VII and X
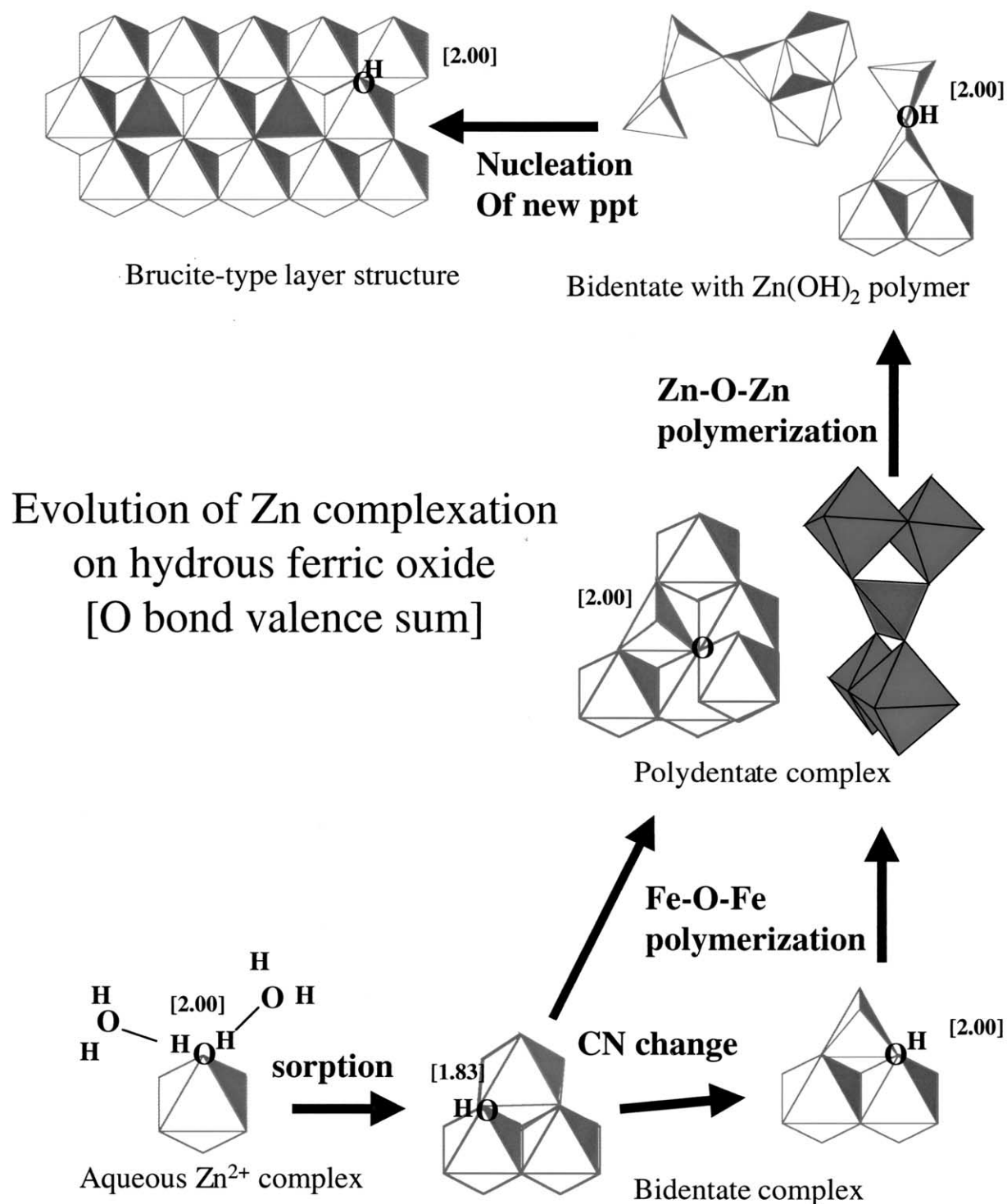
Fig. 15. Molecular models and valence-bond analysis for Zn sorption and precipitation. The oxygens for which the valence sum is calculated are indicated in each cluster. The valence sums assume a valence value of 1.00 for H ions in a hydroxide ligand with no hydrogen bonding and 0.83 for H ions involved in hydrogen bonding with surface waters (Brown, 1981).

in Fig. 2). As Zn solution content increases this process could become more and more likely, even if at much lower concentrations than indicated by the $Zn(OH)_2$ saturation limit. Thus, each tetrahedral Zn unit seeks an equilibrium between its

tendency to form a polymer with other tetrahedral units or complex with octahedral Fe^{3+}.

This hypothesis is further supported by the changes in second shell neighbor coordination with increasing Zn concentra-

tion. The uniform decrease in coordination number was only plausibly explained in our EXAFS fitting analysis by the gradual increase of tetrahedral Zn sites having mainly only tetrahedral Zn second nearest neighbors. Thus, a complete picture is formed for the bulk of our samples: tetrahedral Zn^{2+} is the main Zn unit formed in our samples, and it has a tendency to polymerize as well as form multidentate complexes. With increasing Zn, the polymerization process is enhanced, eventually blocking most of the Zn-Fe complexation. Such polymers must be small and dispersed; otherwise, second neighbor coordination numbers ought to increase at some point, now due to multiple tetrahedral Zn second neighbors. The low Zn-Fe coordination numbers that we observe near Zn/(Zn + Fe) compositions of 0.1 may be due in part to the presence of a wide range of local geometries that escape simple modeling efforts and average out EXAFS amplitudes due to very broad frequency (interatomic distance) ranges. The span of values seen for Zn tetrahedral–tetrahedral topology (Table 1, Fig. 4), which are due to the wide dispersion of Zn-O-Zn angles in these linkages, support this view. With increasing zinc content a change in sorption behavior, or at least irregularities among published data sets, appear at about a Zn/(Zn + Fe) concentration of 0.06 (Fig. 1) in data collected by Kinniburgh and Jackson (1982). Our results show no clear break in behavior near this value, but the extrapolation of fitted coordination numbers (Fig. 13) suggests a major change at Zn/(Zn + Fe) of about 0.2 to 0.3. This composition is close to the intersection of the Kinniburgh and Jackson (1982) isotherm curve with the saturation limit for $Zn(OH)_2$. Our preparation of the high Zn samples was limited and did not attempt to cover all the many possibilities. However, all three samples show clear evidence for substantial octahedral Zn and precipitates or surface complexes with mixed octahedral–octahedral and octahedral–tetrahedral Zn connectivity. This suggests that at least in our samples, higher levels of aqueous Zn lead to the stabilization of a brucite or α-$Zn(OH)_2$–like structure. In the 0.50 Zn/(Zn + Fe) sample, the ratio of second neighbor sites from the EXAFS fitting can be explained only by a brucite-like structure populated with Zn tetrahedra at layer edges. For the pure amorphous $Zn(OH)_2$ samples, there is a reduced second neighbor distance ratio that could be consistent with formation of planar octahedral Zn layers with Zn tetrahedra bonded over (and also perhaps below) vacancies in the layers.

4.3. HFO Surface-Enhanced Precipitation

Once tetrahedral complexation is achieved on the ferrihydrite surface, the formation of tetrahedral-based polymers of one of the $Zn(OH)_2$ structural motifs may be kinetically favored. But is this process a generally important one in sorption reactions? Sorbing species that readily polymerize among themselves in solution appear likely to polymerize on a favorable surface outside of their polymer solution stability range. For example, Fe^{3+} sorption on silica surfaces at pH ranges where Fe^{3+} octahedral dimer or polymer concentrations are expected to be negligible results in polymerization even at very low surface coverages—on the order of a few percent of surface sites (Waychunas et al., 1999). An analogous process with Zn^{2+} could occur and thus would explain why zinc hydroxide polymerization appears to occur at relatively low

sorption coverages on a variety of oxide substrates. This type of behavior is consistent with manifestation of the Ostwald Step Rule (Schindler, 1967; Stumm and Morgan, 1981; Morse and Casey, 1988; Parks, 1990; Stumm, 1992) whereby metastable phases nucleate before stable phases and then slowly convert to more stable forms. Related arguments for continuous sorption-precipitation behavior have been made by Farley et al. (1985) and by James and Healy (1972).

Another aspect of the effect of surface attachment is the change in interaction of complexed species with surface water. Figure 15 shows how the bond valence of octahedral aqueous Zn^{2+} complexes are perfectly balanced if multiple hydrogen bonds with water oxygens are assumed. This situation would render the unit soluble over a wide range of solution conditions. However, if a coordination change occurs as expected, the tetrahedral apical oxygens in contact with water molecules will not have perfect valence satisfaction. The valence sum would equal about 2.16 if two hydrogens were attached to the apical oxygen but also involved in hydrogen bonding, and larger still if they did not form hydrogen bonds. If a single proton is attached to the apical oxygen, then even without any additional hydrogen bonding, the valence sum is 1.50. Such an imbalance would tend to permit formation of Zn(OH)-Zn(OH) tetrahedral linkages because the linkage oxygen with a single bound proton would have perfect valence satisfaction. Thus, the initial sorption and rearrangement would dispose the surface for further polymerization of a tetrahedral zinc precipitate. This process could continue with increasing zinc in solution until nucleation of an octahedral planar zinc hydroxide structure is favored. Hence, in this system, surface complexation geometry is dictated by at least four competing processes: sorption and transformation of octahedral Zn into tetrahedral Zn, Fe-O-Fe polymerization, Zn-OH-Zn polymerization, and nucleation of mainly octahedral Zn layer structures at high Zn solution levels.

4.4. Applications to Soil Chemistry and Other Systems

Our experiments were carried out with the exclusion of atmospheric CO_2 and thus are most applicable to low carbonate sediments and soils (Coston et al., 1995; Davis et al., 1998). The results demonstrate that surface complexation and precipitation can be responsible for significant amounts of Zn uptake without the nucleation and growth of franklinite spinel. Hence, Zn sequestration predictions based on a bulk franklinite stability criterion may not include a sufficiently large physical range. Further, there appears to be a clear threshold in Zn concentration where the onset of the layer zinc hydroxide structures occurs. This would probably be a rare phenomena in natural soils and sediments given the Zn concentrations required but may have relevance to mine waste dumps where moderate pH levels obtain and to situations where Zn is heterogeneously distributed. Finally, this work indicates the complications that ensue from simultaneous and competing precipitation/complexation reactions. Such phenomena may be largely peculiar to the Zn-HFO system, but the similarity of several other cation sorption isotherms indicate that such behavior may be present at high metal concentrations.

REFERENCES

Abrahams S. C. (1967) Crystal structure of the transition-metal molybdates and tungstates III. Diamagnetic α-ZnMoO$_4$. *J. Chem. Phys.* **46,** 2052–2063.

Allman R. (1968) Verfeinerung der Struktur des Zinkhydroxidchlorids II, Zn$_5$(OH)$_8$Cl$_2 \cdot$ H$_2$O. *Zeit. Krist.* **126,** 417–426.

Ankudinov A. L., Zabinsky S. I., and Rehr J. J. (1996) Single configuration Dirac-Fock atom code. *Comp. Phys. Comm.* **98,** 359–364.

Ankudinov A. L. and Rehr J. J. (1997) Relativistic spin-dependent X-ray absorption spectra. *Phys. Rev. B*56, R1712–R1715.

Ankudinov A. L., Ravel B., Rehr J. J., and Conradson S. D. (1998) Real space multiple scattering calculation and interpretation of X-ray–absorption near-edge structure. *Phys. Rev. B* **58,** 7565–7576.

Ansell G. B. and Katz L. (1966) A refinement of the crystal structure of zinc molybdenum (IV) oxide, Zn$_2$Mo$_3$O$_8$. *Acta Cryst.* **21,** 482–488.

Baes C. F. and Mesmer R. E. (1976) *The Hydrolysis of Cations.*Krieger.

Bear I. J., Grey I. E., Madsen I. C., Newnham I. E., and Rogers L. J. (1986) Structures of the basic zinc sulfates 3Zn(OH)$_2 \cdot$ ZnSO$_4 \cdot$ mH$_2$O, m = 3 and 5. *Acta Cryst.* **B42,** 32–39.

Benjamin M. M. (1978) Effects of competing metals and complexing ligands on trace metal adsorption at the oxide/solution interface. Ph.D. thesis. Stanford University.

Benjamin M. M. and Leckie J. O. (1981) Multiple-site adsorption of Cd, Cu, Zn and Pb on amorphous iron oxyhydroxide. *J. Colloid Interface Sci.* **79,** 209–221.

Bochatay L. and Persson P. (2000) Metal ion coordination at the water–manganite (γ-MnOOH) interface. *J. Coll. Interface Sci.* **229,** 593–599.

Boehm H. P., Steinle J., and Vieweger C. (1977) [Zn$_2$Cr(OH)$_6$]X $\cdot$ 2H$_2$O, New layer compounds capable of anion exchange and intracrystalline swelling. *Angew. Chem. Int. Ed. Engl.* **16,** 265–266.

Brown I. D. (1981) The bond-valence method; an empirical approach to chemical structure and bonding. In *Structure and Bonding in Crystals*(ed. M. O'Keeffe), Vol. 2, pp. 1–30. Academic Press.

Cain K. J., Melendres C. A., and Maroni V. A. (1987) Raman and ^{67}Zn NMR studies of the structure of zinc (II) solutions in concentrated aqueous potassium hydroxide. *J. Electrochem. Soc.* **134,** 519–524.

Calvo C. (1963) The crystal structure and luminescence of γ-zinc orthophosphate. *J. Phys. Chem. Solids.* **24,** 141–149.

Christensen A. N. (1969) The crystal structure of γ-Zn(OH)$_2$. *Acta Chim. Scand.* **23,** 2016–2020.

Cocco G., Fanfani L., and Zanazzi P. F. (1966) The crystal structure of tarbuttite, Zn$_2$(OH)PO$_4$. *Zeit. Krist.* **123,** 321–329.

Coston J. A., Fuller C. C., Davis J. A. (1995) Pb^{2+} and Zn^{2+} adsorption by a natural aluminum- and iron-bearing surface coating on an aquifer sand. *Geochim. Cosmochim. Acta* **59,** 3535–3547.

Davis J. A., Coston J. A., Kent D. B., and Fuller C. C. (1998) Application of the surface complexation concept to complex mineral assemblages. *Environ. Sci. Technol.* **32,** 2820–2828.

DeRoy A., Besse J. P., and Bondot P. (1985) Structural approach and conductivity of lamellar hydroxides Zn$_2$Cr(OH)$_6$X $\cdot$ nH$_2$O (X = anion) by XANES, EXAFS and X-ray diffraction. *Mater. Res. Bull.* **20,** 1091–1098.

Dietrich H. G. and Johnston J. (1927) Equilibrium between crystalline zinc hydroxide and aqueous solutions of ammonium hydroxide and of sodium hydroxide. *J. Am. Chem. Soc.* **49,** 1419–1425.

Dzombak D. A. and Morel F. M. M. (1986) Sorption of cadmium on

hydrous ferric oxide at high sorbate/sorbent ratios: Equilibrium, kinetics, and modeling. *J. Coll. Interface Sci.* **112,** 588–598.

Effenberger H., Mereiter K., and Zemann J. (1981) Crystal structure refinements of magnesite, calcite, rhodochrosite, siderite, smithsonite and dolomite, with discussion of some aspects of the stereochemistry of calcite-type carbonates. *Zeit. Krist.* **156,** 233–243.

Eriksson L., Louer D., and Werner P. -E. (1989) Crystal Structure determination and Rietveld refinement of Zn(OH)(NO$_3$)H$_2$O. *J. S. S. Chem.* **81,** 9–20.

Farley K. J., Dzombak D. A., and Morel F. M. M. (1985) A surface precipitation model for the sorption of cations on metal oxides. *J. Coll. Interface Sci.* **106,** 226–242.

Feitknecht W. (1938) Über die α-Form der hydroxyde zweiwertiger metalle. *Helv. Chim. Acta* **21,** 766–784.

Fuller C. C., Davis J. A., and Waychunas G. A. (1993) Surface chemistry of ferrihydrite. 2. Kinetics of arsenate adsorption and coprecipitation. *Geochim. Cosmochim. Acta* **57,** 2271–2282.

George G. and Pickering I. (1995) EXAFSPAK, a suite of computer programs for the analysis of X-ray absorption spectra. Stanford Synchrotron Radiation Laboratory.

Gerth J. (1990) Unit-cell dimensions of pure and trace metal-associated goethites. *Geochim. Cosmochim. Acta* **54,** 363–371.

Ghose S. (1964) The crystal structure of hydrozincite. *Acta Cryst.* **17,** 1051–1057.

Giester G. and Rieck B. (1996) Bechererite, (Zn,Cu)$_6$Zn$_2$(OH)$_{13}$ [(S,Si)(O,OH)$_4$]$_2$, a novel mineral species from the Tonopah-Belmont Mine, Arizona. *Am. Mineral.* **81,** 244–248.

Grice J. D. and Dunn P. J. (1989) Sclarite, a new mineral from Franklin, New Jersey, with essential octahedrally and tetrahedrally coordinated zinc: Description and structure refinement. *Am. Mineral.* **74,** 1355–1359.

Groat L. A. (1996) The crystal structure of namuwite, a mineral with Zn in tetrahedral and octahedral coordination, and its relationship to the synthetic basic zinc sulfates. *Am. Mineral.* **81,** 238–243.

Harvey D. T., Fulghum J. E., and Linton R. W. (1983) Determination of adsorption soichiometry for zinc adsorption on amorphous hydrous ferric oxide. *J. Coll. Interface Sci.* **94,** 276–278.

Harvey D. T. and Linton R. W. (1984) X-ray Photoelectron spectroscopy (XPS) of adsorbed zinc on amorphous hydrous ferric oxide. *Colloids Surf.* **11,** 81–96.

Hawthorne F. C. (1976) A refinement of the crystal structure of Adamite. *Can. Mineral.* **14,** 143–148.

Hill R. J. (1981) The structure of loseyite. *Acta Cryst.* **B37,** 1323–1328.

Hill R. J., Craig J. R., and Gibbs G. V. (1979) Systematics of the spinel structure type. *Phys. Chem. Minerals* **4,** 317–339.

Iitaka Y., Locchi S., and Oswald H. R. (1962) Die Kristallstruktur von Zink-hydroxidsulfat I. Zn(OH)$_2 \cdot$ ZnSO$_4$. *Acta Cryst.* **15,** 559–563.

James R. O. and Healy T. W. (1972) Adsorption of hydrolyzable metal ions at the oxide–water interface. II. charge reversal of SiO$_2$ and TiO$_2$ colloids by adsorbed Co(II), La(III), and Th(IV) as model systems. *J. Coll. Interface Sci.* **40,** 53–64.

Jenne E. A. (1968) Controls on Mn, Fe, Co, Ni, Cu and Zn concentrations in soils and water: The significant role of hydrous Mn and Fe oxides. *Adv. Chem. Soc.* **73,** 337–387.

Kihara K. and Donnay G. (1985) Anharmonic thermal vibrations in ZnO. *Can. Mineral.* **23,** 647–654.

Kinniburgh D. G. and Jackson M. L. (1982) Concentration and pH dependence of calcium and zinc adsorption by iron hydrous oxide gel. *Soil Sci. Soc. Am. J.* **46,** 56–61.

Klaska K.-H., Eck J. C., and Pohl D. (1978) New investigation of willemite. *Acta Cryst.* **B34,** 3324–3325.

Lindsay W. L. (1979) *Chemical Equilibria in Soils.* Wiley-Interscience.

Louer M., Grandjean D., and Weigel D. (1973) Etude structurale des hydroxynitrates de nickel et de zinc. II. Structure cristalline du nitrate basique de zinc, 2Zn(OH)$_2 \cdot$ Zn(NO$_3$)$_2$. *Acta Cryst.* **B29,** 1703–1706.

Manceau A. and Combes J.-M. (1988) Structure of Mn and Fe oxides and hydroxides: A topological approach by EXAFS. *Phys. Chem. Minerals* **15,** 283–295.

Manceau A., Lanson B., Schlegel M. L., Harge J. C., Musso M., Eyebert-Berard L., Hazemann J. L., Chateigner D., and Lamble G. M. (2000a) Quantitative Zn speciation in smelter-contaminated soils by EXAFS spectroscopy. *Am. J. Sci.* **300,** 289–343.

Manceau A., Schlegel M. L., Musso M., Sole V. A., Gauthier C., Petit P. E., and Trolard F. (2000b) Crystal chemistry of trace elements in natural and synthetic goethite. *Geochim. Cosmochim. Acta* **64,** 3643–3662.

McCarroll W. H., Katz L., and Ward R. (1957) Some ternary oxides of tetravalent molybdenum. *J. Am. Chem. Soc.* **79,** 5410–5414.

Morse J. W. and Casey W. H. (1988) Ostwald processes and mineral paragenesis in sediments. *Am. J. Sci.* **288,** 537–560.

O'Day P. A., Carroll S. A., and Waychunas G. A. (1998) Rock–water interactions controlling zinc, cadmium, and lead concentrations in surface waters and sediments, U.S. Tri-State Mining District. 1. Molecular identification using X-ray absorption spectroscopy. *Environ. Sci. Technol.* **32,** 943–955.

Pandya K. I., Russell A. E., McBreen J., and O'Grady W. E. (1995) EXAFS Investigations of Zn(II) in concentrated aqueous hydroxide solutions. *J. Phys. Chem.* **99,** 11967–11973.

Parkhurst D. L. (1985) The application of EXAFS and mean-activity coefficient data to ion-association models for the zinc–chloride system. M.S. thesis. Stanford University.

Parks G. A. (1990) Surface energy and adsorption at mineral/water interfaces: An introduction. *Rev. Mineral.* **23,** 133–176.

Pavlov M., Siegbahn P. E. M., and Sandström M. (1998) Hydration of beryllium, magnesium, calcium, and zinc ions using density functional theory. *J. Phys. Chem.* **A102,** 219–228.

Plieth K. and Sänger G. (1967) Die Struktur des Stranskiite $Zn_2Cu(AsO_4)_2$. *Zeit. Krist.* **124,** 91–100.

Porta P., Morpurgo S., and Pettiti I. (1996) Characterization by X-ray absorption, X-ray powder diffraction, and magnetic susceptibility of Cu-Zn-Co-Al-containing hydroxycarbonates, oxycarbonates, oxides, and their products of reduction. *J. Solid State Chem.* **121,** 372–378.

Reddy K. J., Sullivan P. J., and Yelton J. L. (1988) Solubility relationships of zinc associated with acid mine drainage. *J. Environ. Qual.* **17,** 712–714.

Rehr J. J., Zabinsky S. I., and Albers R. C. (1992) High-order multiple scattering calculations of X-ray–absorption fine structure. *Phys. Rev. Lett.* **69,** 3397–3400.

Robert J.-L. and Gasperin M. (1985) Crystal structure refinement of hendricksite, a Zn- and Mn-rich trioctahedral potassium mica: A contribution to the crystal chemistry of zinc-bearing minerals. *Tschermaks Mineral. Petrol. Mitt.* **34,** 1–14.

Sadiq M. (1991) Solubility and speciation of zinc in calcareous soils. *Proc. Int. Conf. Metals Soils Waters Plants Animals* **57–58,** 411–421.

Schindler P. W. (1967) Heterogeneous equilibria involving oxides, hydroxides, carbonates, and hydroxide carbonates. In *Equilibrium Concepts in Natural Water Systems* (ed. W. Stumm), pp. 196–221. American Chemical Society.

Schindler P., Althaus H., and Feitknecht W. (1964) loslichkeitsprodukte und Freie Bildungsenthalpien von Zinkodix, amorphem Zinkhydroxid, β_1-, β_2-, γ-, δ- and ε-Zinkhydroxid. *Helv. Chim. Acta* **47,** 982–991.

Schindler P., Reinert M., and Gamsjager H. (1969) Loslichkeitskonstanten und Freie Bildundsenthalpien von $ZnCO_3$ und $Zn_5(OH)_6(CO_3)_2$ bei 25°. *Helv. Chim. Acta* **52,** 2327–2332.

Schlegel M. L., Manceau A., and Charlet L. (1997) EXAFS study of Zn and Zn EDTA sorption at the goethite-(FeOOH)/water interface. *J. Phys. Coll.* **C2,** 823–824.

Schnering H. G. (1964) Zur Konstitution des ε-$Zn(OH)_2$. *Zeit. Anorg. Allgemein Chem.* **330,** 170–178.

Schulze D. G. (1984) The influence of aluminum on iron oxides. VIII. Unit-cell dimensions of Al-substituted goethites and estimation of Al from them. *Clays Clay Minerals* **32,** 36–44.

Shannon R. D. and Prewitt C. T. (1969) Effective ionic radii in oxides and fluorides. *Acta Cryst.* **B25,** 925–946

Stählin W. and Oswald H. R. (1970) The crystal structure of zinc hydroxide nitrate $Zn_5(OH)_8(NO_3)_2 \cdot 2H_2O$. *Acta Cryst.* **B26,** 860–863.

Stanton D. A. and Burger R. D. (1970) Mechanisms for the reaction of zinc with iron and aluminum oxides. *Agrochemophysica* **2,** 63–75.

Stephens J. S. and Calvo C. (1967) Crystal structure of β-$Zn_3(PO_4)_2$. *Can. J. Chem.* **45,** 2303–2312.

Stern E. A. and Heald S. M. (1979) X-ray filter assembly for fluorescence measurements of X-ray absorption fine structure. *Rev. Sci. Instrum.* **50,** 1579–1582.

Stumm W. (1992) *Chemistry of the Solid–Water Interface.* Wiley.

Stumm W. and Morgan J. J. (1981) *Aquatic Chemistry.* Wiley.

Tossell J. A. (1991) Calculations of the structures, stabilities, and Raman and Zn NMR spectra of $ZnCl_n(OH_2)_{a2-n}$ species in aqueous solution. *J. Phys. Chem.* **95,** 366–371.

Trainor T. P., Brown G. E., and Parks G. A. (2000) Adsorption and precipitation of aqueous Zn(II) on alumina powders. *J. Coll. Interface Sci.* **231,** 359–372.

Vielhaber V. E. and Hoppe R. (1965) Über oxozinkate der alkalimetalle. *Zeit. Anorg. Allgem. Chem.* **338,** 209–221.

Waychunas G. A. (1991) Crystal chemistry of oxides and hydroxides. *Rev. Mineral.* **25,** 11–68.

Waychunas G. A., Rea B. A., Davis J. A., and Fuller C. C. (1993) Surface chemistry of ferrihydrite: I. EXAFS studies of the geometry of coprecipitated and adsorbed arsenate. *Geochim. Cosmochim. Acta* **57,** 2251–2269.

Waychunas G. A., Fuller C. C., Rea B. A., and Davis J. A. (1996) Wide angle X-ray scattering (WAXS) study of "two-line" ferrihydrite structure: Effect of arsenate sorption and counterion variation and comparison with EXAFS results. *Geochim. Cosmochim. Acta* **60,** 1765–1781.

Waychunas G. A., Davis J. A., and Reitmeyer R. (1999) GIXAFS study of Fe^{3+} sorption and precipitation on natural quartz surfaces. *J. Synchrotron Rad.* **6,** 615–617.

Wegmüller F. (1987) Physisorptive behavior of zinc-aquo-hydroxide. *J. Coll. Interface Sci.* **116,** 312–333.

Wells A. F. (1984) *Structural Inorganic Chemistry,* 5th ed. Clarendon Press.

Yongyai Y. P., Kokpol S., and Rode B. M. (1991) Zinc ion in water: intermolecular potential with approximate three-body correction and Monte Carlo simulation. *Chem. Phys.* **156,** 403–412.

Zachara J. M., Kittrick J. A., Dake L. S., and Harsh J. B. (1989) Solubility and surface spectroscopy of zinc precipitates on calcite. *Geochim. Cosmochim. Acta* **53,** 9–19.